

Epitaxy of hexagonal ABO_3 quantum materials

Johanna Nordlander,¹ Margaret A. Anderson,¹ Charles M. Brooks,¹ Megan E. Holtz,² and Julia A. Mundy^{1, a)}

¹⁾*Department of Physics, Harvard University, USA*

²⁾*Department of Metallurgy and Materials Engineering, Colorado School of Mines, USA*

Hexagonal ABO_3 oxides ($A, B = \text{cation}$) are a rich materials class for realizing novel quantum phenomena. Their hexagonal symmetry, oxygen trigonal bipyramid coordination and quasi-two dimensional layering give rise to properties distinct from those of the cubic ABO_3 perovskites. As bulk materials, most of the focus in this materials class has been on the rare earth manganites, $RMnO_3$ ($R = \text{rare earth}$); these materials display coupled ferroelectricity and antiferromagnetic order. In this review, we focus on the thin film manifestations of the hexagonal ABO_3 oxides. We cover the stability of the hexagonal oxides and substrates which can be used to template the hexagonal structure. We show how the thin film geometry not only allows for further tuning of the bulk-stable manganites but also the realization of metastable hexagonal oxides such as the $RFeO_3$ that combine ferroelectricity with weak ferromagnetic order. The thin film geometry is a promising platform to stabilize additional metastable hexagonal oxides to search for predicted high-temperature superconductivity and topological phases in this materials class.

^{a)}Electronic mail: mundy@fas.harvard.edu

I. INTRODUCTION

Complex oxides display some of the most exotic physical states known. The subtle interplay of Coulomb interactions, electron-lattice coupling and spin/orbital ordering gives rise to phenomena as diverse as high-temperature superconductivity and ferromagnetism. Synthesizing complex oxides in the thin film form offers further opportunities to tune the ground state. Here, strain imparted from a substrate, dimensionality in a superlattice architecture, or charge transfer/coupling at an interface can unleash further emergent properties not present in the parent compounds^{1,2}. Moreover, complex oxide thin films not only offer opportunities to study diverse physical phenomena but could be harnessed for a number of next-generation applications³.

To date, however, much of the work on complex oxides in the thin film form has focused on cubic perovskite oxides. This review focuses on a different class of oxides with the same ABO_3 stoichiometry ($A, B =$ cations), the hexagonal oxides. As shown in Fig 1(a), the crystal structure differs from that of the cubic perovskites: the B -site cation is surrounded by a trigonal bipyramid arrangement of oxygen atoms in contrast to the oxygen octahedra characteristic of the perovskite oxides. Planes of corner-sharing trigonal bipyramids are layered with planes of the A -site cation in a quasi-two-dimensional structure. (We refer the reader to an excellent recent review⁴ that covers a more generic class of hexagonal oxides that include face-sharing polyhedra and other structural types.) We focus on this class of materials not to generically expand the study of oxide compounds, but specifically because the distinct symmetry and the crystal field environment can offer unique opportunities to realize novel properties not present in the cubic perovskite oxides.

While considerably less studied than the perovskite oxides, the hexagonal ABO_3 materials also display a rich array of physical phenomena (see overview in Table I). The most commonly studied hexagonal oxides are the rare earth manganites, $RMnO_3$ where $R =$ Sc, Y, In, Dy–Lu. These materials display robust improper ferroelectricity well above room temperature^{5,6} as a consequence of a lattice trimerization involving a coordinated tilting of the MnO_5 bipyramids and a distortion of the rare earth ion layers^{7,8}, see Fig. 1. Notably, this ferroelectricity coexists and is coupled with antiferromagnetic order^{9–13}, as shown in Fig. 2. More recently, the hexagonal $RFeO_3$ compounds have been studied^{14–16}: in these compounds there is a proposed coupling of ferroelectricity with weak ferromagnetic order¹⁷. In

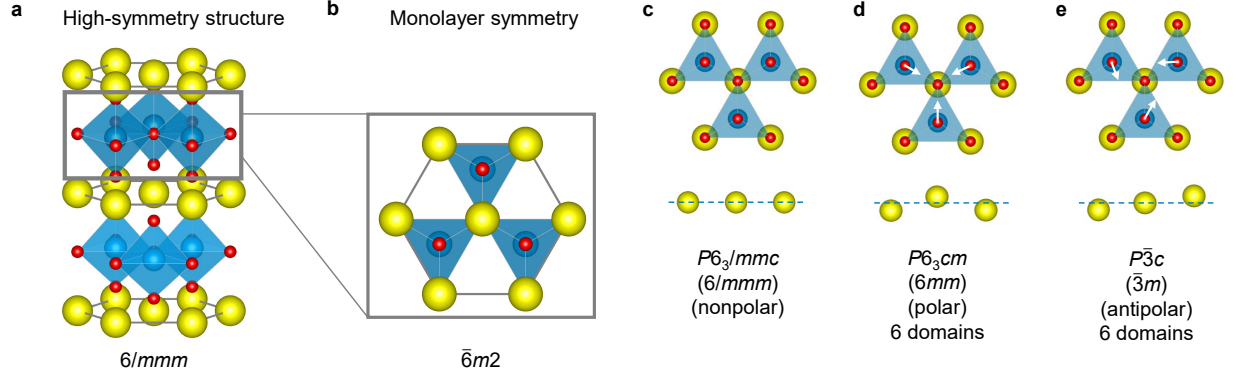


FIG. 1. Crystal structure and symmetry of the hexagonal ABO_3 compounds. The A -site, B -site and oxygen atoms are shown in yellow, blue and red, respectively. (a) The parent centrosymmetric $P6_3/mmc$ structure that is non-polar with point symmetry $6/m\bar{m}m$. (b) A slice of the half-unit-cell plane as indicated in the box in (a), projected down the $[001]$ crystallographic zone axis. The B -site cations sit on a trigonal lattice with a locally lowered (noncentrosymmetric) symmetry compared to the full unit cell structure, which consists of two of these B -site planes rotated 60° with respect to each other, sandwiched between the triangular rare-earth layers. (c)-(e) Displacement patterns found in hexagonal ABO_3 compounds and the corresponding unit-cell space (point) symmetry groups. (c) The nonpolar parent structure, for reference. (d) The polar phase has a coordinated tilting of three BO_5 trigonal bipyramids towards a trimerization center accompanied by a “down-up-down” displacement pattern of A -site ions along the c axis. (e) The antipolar phase consists of intermediate tilt angles 30° away from the polar structure and a “down-middle-up” displacement pattern on the A -site along the c axis.

in addition to proposed uses in energy-efficient magnetoelectric spin-orbit logic devices¹⁸, the ferroelectricity and ferroelectric domain walls in the hexagonal manganites have emerged as fascinating model systems to study diverse physical phenomena. The ferroelectric domain walls display tunable metallic conductivity^{19–21}. The emergence of the ferroelectric domain structure, exhibiting a topologically protected vortex pattern, is further a platform to explore the Kibble-Zurek framework and spontaneous symmetry breaking in a condensed matter system^{22–24}. The structural phase transitions also have been proposed to display Higgs and Goldstone physics²⁵.

In addition to multiferroics, the hexagonal ABO_3 family offers additional prospects to

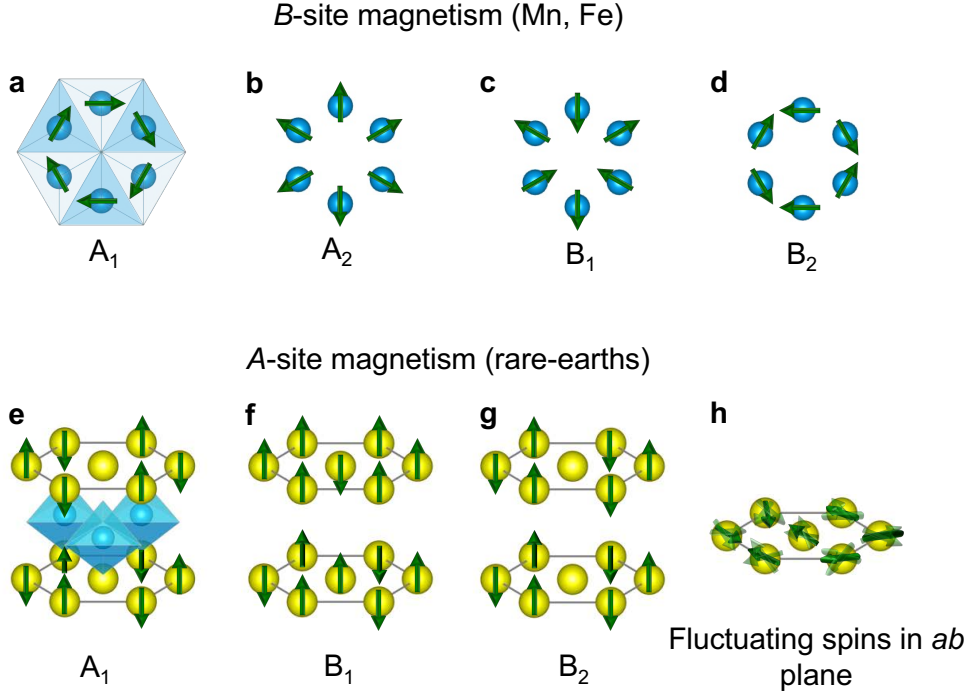


FIG. 2. Magnetic order in the hexagonal ABO_3 compounds. (a)-(d) Spin orientation on the B -site. (e)-(h) Spin orientation on the A -site, for A = rare-earth element. The fully ferromagnetically ordered A_2 configuration is not shown. (h) In the absence of B -site magnetism, the geometric frustration experienced by the rare-earth moments on the triangular lattice can lead to suppressed ordering temperatures or spin fluctuations persistent to the lowest temperatures.

stabilize emergent magnetic ground states including the elusive quantum spin liquid state. In a quantum spin liquid, spins are highly correlated and strongly frustrated due to the crystal symmetry (e.g., triangular, honeycomb or Kagome). The resulting degeneracy between competing ground state spin configurations leads to a highly entangled state that resists macroscopic magnetic ordering to the lowest temperatures²⁶. Importantly, the “spinon” quasiparticle excitations of this system can be itinerant Majorana fermions with a gapless dispersion of relevance to quantum computing²⁷. In addition to the intrinsic triangular symmetry of the hexagonal ABO_3 oxides, chemical doping or lattice distortions can construct a honeycomb and Kagome lattice with additional opportunities to realize frustrated magnetism. For example, $\text{InCu}_{2/3}\text{V}_{1/3}\text{O}_3$ has both Cu^{2+} and V^{5+} on the B -site lattice. These cations in the two:one ratio arrange such that the Cu^{2+} forms a honeycomb lattice^{28,29} as shown in Fig. 3(b). Here, the honeycomb Cu^{2+} atoms seem to order antiferromagnetically³⁰

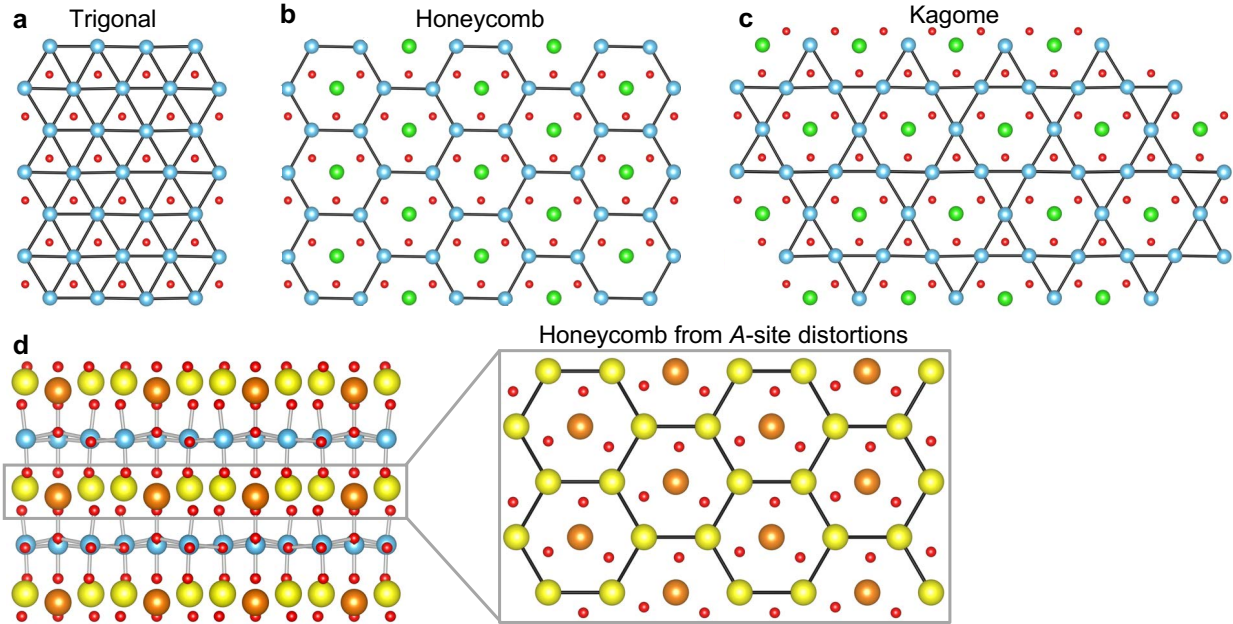


FIG. 3. Symmetry embedded in the ABO_3 structure. (a) A slice of the B -site plane from the ABO_3 structure, projected down the $[001]$ crystallographic zone axis. The B -site cations follow a trigonal pattern. (b),(c) Replacement of the B -site cation with a different element at $1/4$ or $1/3$ filling can construct a honeycomb or kagome lattice, respectively. (d) The honeycomb lattice is also formed on the A -site of the $P6_3cm$ structure where the blue atoms are displaced up and the green atoms displaced down in the "up-up-down" polarization direction. Oxygen in red, A -site cations in yellow/orange and B -site cations in blue/green.

rather than behave as a quantum spin liquid. (This system could also be proximate to chiral superconductivity³¹). In the $LaCu_{3/4}Mo_{1/4}O_3$ compound, the three:one ratio of Cu^{2+} to Mo^{6+} generates a Kagome arrangement of copper atoms³² depicted in Fig. 3(c). Finally, we note that the "up-up-down" ferroelectric trimerization on the A -site generates a honeycomb arrangement as well³³ as shown in Fig. 3(d). In $TbInO_3$, the resulting magnetic frustration on the terbium sub-lattice leads to a lack of order to the lowest temperatures and $TbInO_3$ is a promising quantum spin liquid candidate³³.

Finally, the hexagonal oxides have distinct oxygen sublattices to their perovskite counterparts. In contrast to the oxygen octahedra characteristic of the perovskites, the trigonal bipyramid intrinsic to the hexagonal ABO_3 structure has two distinct oxygen atoms located at the apical and in-plane coordinations. These oxygen atoms can have different

Compound	Properties	References
$RMnO_3$, $R = \text{Sc, Y, Dy-Lu}$	Multiferroic	12
$RMnO_3$, $R = \text{Sc, Y, Dy-Lu}$	Photovoltaic	37,38
$YIn_{1-x}Mn_xO_3$	Blue pigment	39
$DyMnO_3$	Ion/electron conductor	35
$RMnO_3$	oxygen storage	35,40
$RFeO_3$, $R = \text{Lu, Yb, Sc}$	Multiferroic	14–16
$DyFeO_3$	Antiferroelectric	41
$YFeO_3$, $InFeO_3$	Photocatalyst/water splitting	42–44
R_2CuTiO_6 , $R = \text{Y, Dy, Ho, Er, and Yb}$	High- κ dielectric	45
$TbInO_3$	Quantum spin liquid candidate	33,46
$YCrO_3$, YVO_3	Predicted topological semi-metal	47
$YNiO_3$	Predicted superconductor	36,48

TABLE I. Observed and predicted properties of the ABO_3 hexagonal materials.

bonding to the transition metal atom³⁴, which in principle can be harnessed for oxygen ion conductivity³⁵. There have also been theoretical predictions that the crystal field splitting surrounding the transition metal oxide could be harnessed to stabilize superconductivity in hexagonal nickelates (mimicking the electronic structure of the superconducting cuprates and pnictides)³⁶.

Thin film manifestations of these hexagonal oxides offer further opportunities to not only scale down the materials to fundamental thickness limits⁴⁹ and heterostructure them to realize additional functional properties⁵⁰, but furthermore to exploit epitaxy and layering⁵¹ to stabilize metastable compounds. Thin film epitaxy of the hexagonal ABO_3 oxides offers additional challenges in comparison to the cubic perovskite oxides. In this review, we first summarize the stability of the hexagonal ABO_3 compounds. We then describe the thin film deposition of the bulk-stable $RMnO_3$ compounds, including the lattice matching of the hexagonal crystal structure to commercially available substrates. We finally discuss the use of epitaxy to expand the stability of this phase.

II. STABILITY OF THE HEXAGONAL ABO₃ PHASE

Compounds with the ABO₃ stoichiometry can form a variety of cubic, orthorhombic, and hexagonal phases. The formation of the hexagonal phase is dictated by both structural stability and the electronic energy of the *B*-site in the trigonal bipyramid oxygen coordination complex. The structural stability of the competing cubic perovskite phase can be estimated with the tolerance factor (*t*), a geometric quantity based on the ionic radii (*r*) of constituent atoms that indicates how well a given ABO₃ compound fits in the cubic perovskite structure. Here, *t* is given by:

$$t = \frac{(1/\sqrt{2})\text{face diagonal}}{\text{unit cell length}} = \frac{r_A + r_O}{\sqrt{2}(r_B + r_O)}$$

The tolerance factor is 1 for *A* and *B* ions which can be packed into a perfect cubic perovskite. The well-known perovskite SrTiO₃ has *t*=1.01, when calculated with $r_A = r_{\text{Sr}^{2+}(XII)} = 144$ pm, $r_B = r_{\text{Ti}^{4+}(VI)} = 60.5$ pm, and $r_O = r_{\text{O}^{2-}(II)} = 135$ pm where $r_{\text{Sr}^{2+}(XII)}$ is the ionic radius of Sr²⁺ with twelve-fold oxygen coordination⁵². As *t* deviates from 1, the structure is distorted from a cubic perovskite (Fig. 4). For example, YCrO₃ with *t*=0.83, forms a distorted orthorhombic perovskite phase. A tolerance factor far from 1 does not imply the stability of the hexagonal phase, but instead identifies candidate compounds that are less stable in the cubic perovskite phase. YMnO₃ and YFeO₃, both with *t*=0.81, have less structural stability in the cubic perovskite phase.

Despite having the same tolerance factor, YFeO₃ assumes an orthorhombic perovskite structure whereas YMnO₃ crystallizes in a hexagonal phase. In addition to the structural stability of competing phases, electronic stability impacts the bulk stable crystal structure. The electronic stability of the hexagonal oxides is based on the crystal field splitting of the *d*-orbitals of the *B*-site transition metal ions with trigonal bipyramid (five-fold) oxygen coordination. With this ligand geometry, the five *d*-orbitals split into three energy levels: two doubly degenerate lower energy levels and one non-degenerate high energy level (Fig. 5). In contrast, a perovskite with octahedral (six-fold) coordination on the *B*-site has two energy levels: the three-fold degenerate *t*_{2g} low energy level and the doubly degenerate *e*_g high energy level. Fe³⁺, with the electron configuration [Ar]3d⁵, is more stable in the octahedral coordination, which avoids occupying the highest energy level in the trigonal bipyramid configuration. As a result, RFeO₃ compounds are more stable as orthorhombic perovskites. In contrast, Mn³⁺, with configuration [Ar]3d⁴, is more stable in a trigonal

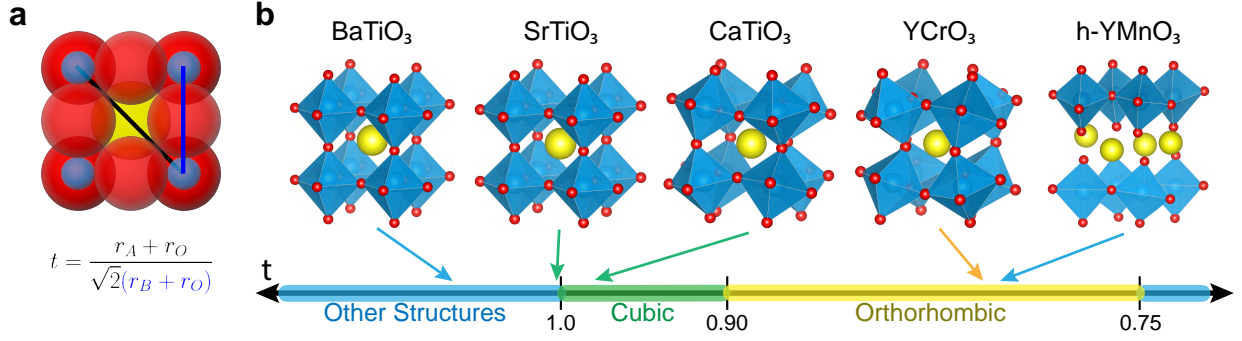


FIG. 4. The perovskite Goldschmidt tolerance factor. (a) The tolerance factor, t , is calculated as the ratio of $\frac{1}{\sqrt{2}}$ times a face diagonal ($2r_A + 2r_O$) and a unit cell length ($2r_B + 2r_O$). $t = 1$ for ions which perfectly pack into the cubic perovskite structure. (b) Examples of ABO_3 compounds with various tolerance factors and the approximate regions of stability for each structure. As t decreases from 1, the B -site octahedral cages tilt and bond lengths change forming successively lower-symmetry structures. The cubic perovskite phase with space group $Pm\bar{3}m$ occurs for approximately $0.90 < t < 1.0$, while the orthorhombic phase with space group $Pnma$ or $Pbnm$ occurs for $0.75 < t < 0.90$ ⁵³. Outside of this range, other structures including a hexagonal phase with space group $P6_3cm$, a tetrahedral phase, and the hexagonal ilmenite structure are formed. The tolerance factors for $BaTiO_3$, $SrTiO_3$, $CaTiO_3$, $YCrO_3$, and $YMnO_3$ are 1.07, 1.01, 0.97, 0.83, and 0.81, respectively.

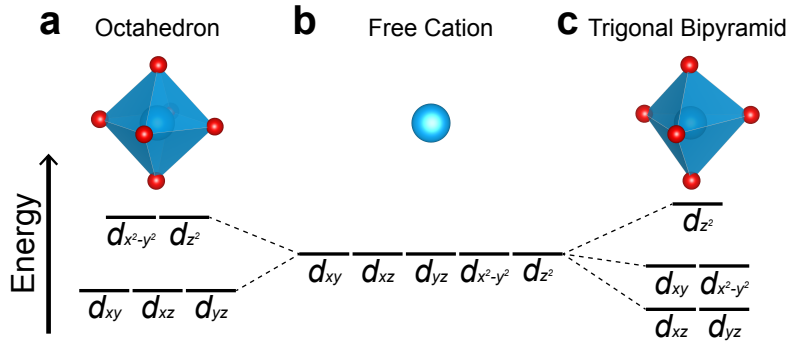


FIG. 5. The d -orbital energy configuration for ions with (a) octahedral oxygen coordination (as for B -site cations in cubic perovskites), (b) free ions, and (c) trigonal bipyramid coordination (as for B -site cations in hexagonal ABO_3 materials).

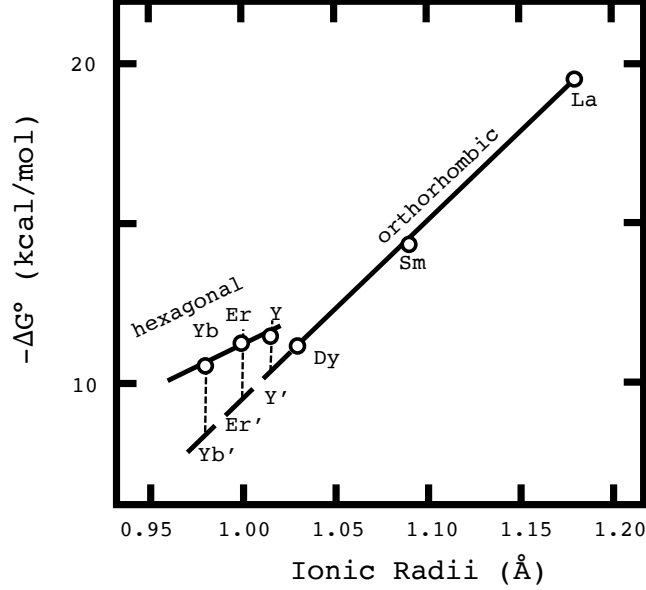


FIG. 6. The dependence of free energy of formation on rare-earth ionic radii, RE^{3+} in $RMnO_3$, at 1200° . RE' indicates the estimated free energy of formation for the perovskite structure in high pressure. Reprinted with permission from Kamata *et al.* Mater. Res. Bull. **14**, 1007-1012 (1979). Copyright 1979 Elsevier.⁵⁵

bipyramid complex where the four valence electrons populate the four lower energy orbitals. With octahedral coordination, Mn^{3+} forms a degenerate high-spin state with its fourth valence electron in either of the two e_g orbitals; these perovskite manganites are Jahn-Teller active⁵⁴. The electron in the higher energy orbitals lowers the stability of the compound. Thus, the $RMnO_3$ compounds form a hexagonal crystal structure for small R ($R = Sc, Y, Dy-Lu$) as shown in Fig. 6.

In Fig. 7, we summarize the elements which have been found in the hexagonal ABO_3 polymorph. In contrast to the cubic perovskites where almost every element on the periodic table can occupy one of the three lattice sites^{2,56}, the hexagonal structure can form with more limited chemical compositions. Only six cations are known to fully occupy the B -site although there are much wider range of elements which can be stabilized as dopants or as partial occupants of this lattice site. We note that thin film stabilization is a powerful platform for synthesizing phases which are metastable as bulk crystals⁵⁷. While $YMn_{1-x}Fe_xO_3$ could be stabilized in the $P6_3cm$ structure for $x < 0.3$ in bulk crystals, epitaxial stabilization has led to the construction of $LuFeO_3$ with the hexagonal $P6_3cm$ structure^{14-16,58}. Explicit

Hexagonal ABO_3

H																	He
Li	Be											B	C	N	O	F	Ne
Na	Mg											Al	Si	P	S	Cl	Ar
K	Ca	Sc	Ti	V	Cr	Mn	Fe	Co	Ni	Cu	Zn	Ga	Ge	As	Se	Br	Kr
Rb	Sr	Y	Zr	Nb	Mo	Tc	Ru	Rh	Pd	Ag	Cd	In	Sn	Sb	Te	I	Xe
Cs	Ba		Hf	Ta	W	Re	Os	Ir	Pt	Au	Hg	Tl	Pb	Bi	Po	At	Rn
Fr	Ra		Rf	Db	Sg	Bh	Hs	Mt	Ds	Rg	Cn	Nh	Fl	Mc	Lv	Ts	Og

La	Ce	Pr	Nd	Pm	Sm	Eu	Gd	Tb	Dy	Ho	Er	Tm	Yb	Lu
Ac	Th	Pa	U	Np	Pu	Am	Cm	Bk	Cf	Es	Fm	Md	No	Lr

 A-site ion	 A-site dopant	 B-site ion	 B-site dopant
--	--	--	--

FIG. 7. Periodic table indicating the elements that can be stabilized in the hexagonal ABO_3 phase. A-site ions are colored in yellow and B-site ions are colored in blue. We color in light blue/yellow the elements which can be found as dopants or to partially occupy the site.

stromataxy – precise control over the layering – has enabled further stability of this phase⁵¹.

III. SUBSTRATE TEMPLATES FOR HEXAGONAL ABO_3 THIN FILMS

While sputtering, metal-organic chemical vapor deposition (MOCVD), molecular-beam epitaxy (MBE) and pulsed laser deposition (PLD) have emerged as powerful tools to synthesize oxide materials in the film form, there are unique challenges to the deposition of hexagonal oxides. In contrast to the more commonly studied perovskite oxides, where there is a “menu” of isostructural, commercially available perovskite substrates⁵⁹ with various lattice constants, the most readily available oxide substrate used to stabilize hexagonal films is Al_2O_3 . This substrate is not well lattice-matched to all desired hexagonal ABO_3 films. In addition to hexagonal oxides, cubic substrates can be used in the (111) orientation. Figure 8 shows the mismatch between the prototypical $YMnO_3$ and (0001) Al_2O_3 , (111) cubic oxides MgO , $MgAl_2O_4$, $(ZrO_2)_{0.905}(Y_2O_3)_{0.095}$ (9.5.mol% yttria-stabilized zirconia, YSZ), and (111) oriented metallic platinum. In addition to directly aligning on the substrate, the $YMnO_3$

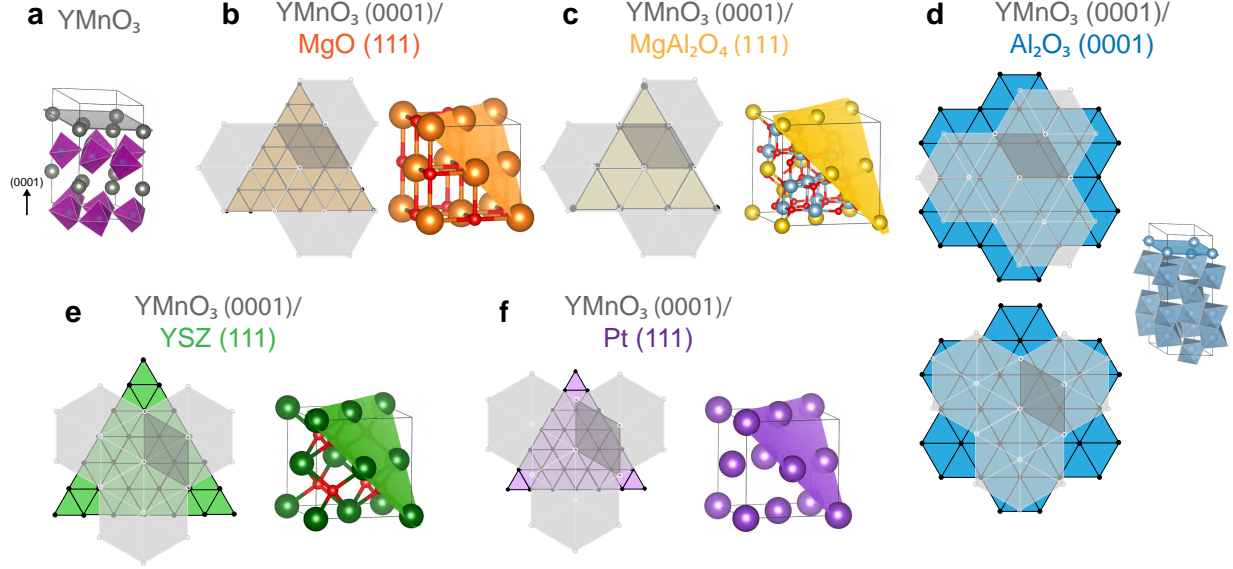


FIG. 8. Lattice matching between YMnO_3 and common substrates. (a) The structure of YMnO_3 with a (0001) plane unit cell of yttrium atoms highlighted in grey. (b) Lattice matching between yttrium atoms in the (0001) plane of YMnO_3 in grey and the magnesium atoms in the (111) plane of MgO in orange. Lattice mismatch (with a factor of 2): -2.9%. (c) Lattice mismatch between YMnO_3 in grey and the magnesium atoms of MgAl_2O_4 (111) in yellow. Lattice mismatch: -7.0%. (d) Lattice mismatch of YMnO_3 with the blue aluminum atoms of $\text{Al}_2\text{O}_3(0001)$ in two orientations: aligned (Lattice mismatch (with a factor of $\frac{4}{3}$): 3.4%) and with a 30° rotation (Lattice mismatch (with a factor of $\frac{2}{3}$): -10.5%). (e) Lattice mismatch between 30° rotated YMnO_3 and the zirconium atoms of yttria-stabilized zirconia (YSZ) in green. Yttrium is omitted from the YSZ crystal structure for clarity. Lattice mismatch: 2.6%. (f) Lattice mismatch between 30° rotated YMnO_3 and the platinum atoms of $\text{Pt}(111)$. Lattice mismatch (with a factor of $\frac{4}{3}$): 4.6%.

could also adopt a 30° rotation with respect to the substrate orientation (this would be analogous to the 45° rotation cubic perovskites might assume in the (001) direction). Figure 9 summarizes the lattice matching between the $P6_3cm$ YMnO_3 and many commercially available substrates. While (111)-oriented cubic perovskites also have the correct symmetry, our experience is that these substrates seed the (111)-perovskite film rather than the intended hexagonal polymorph.

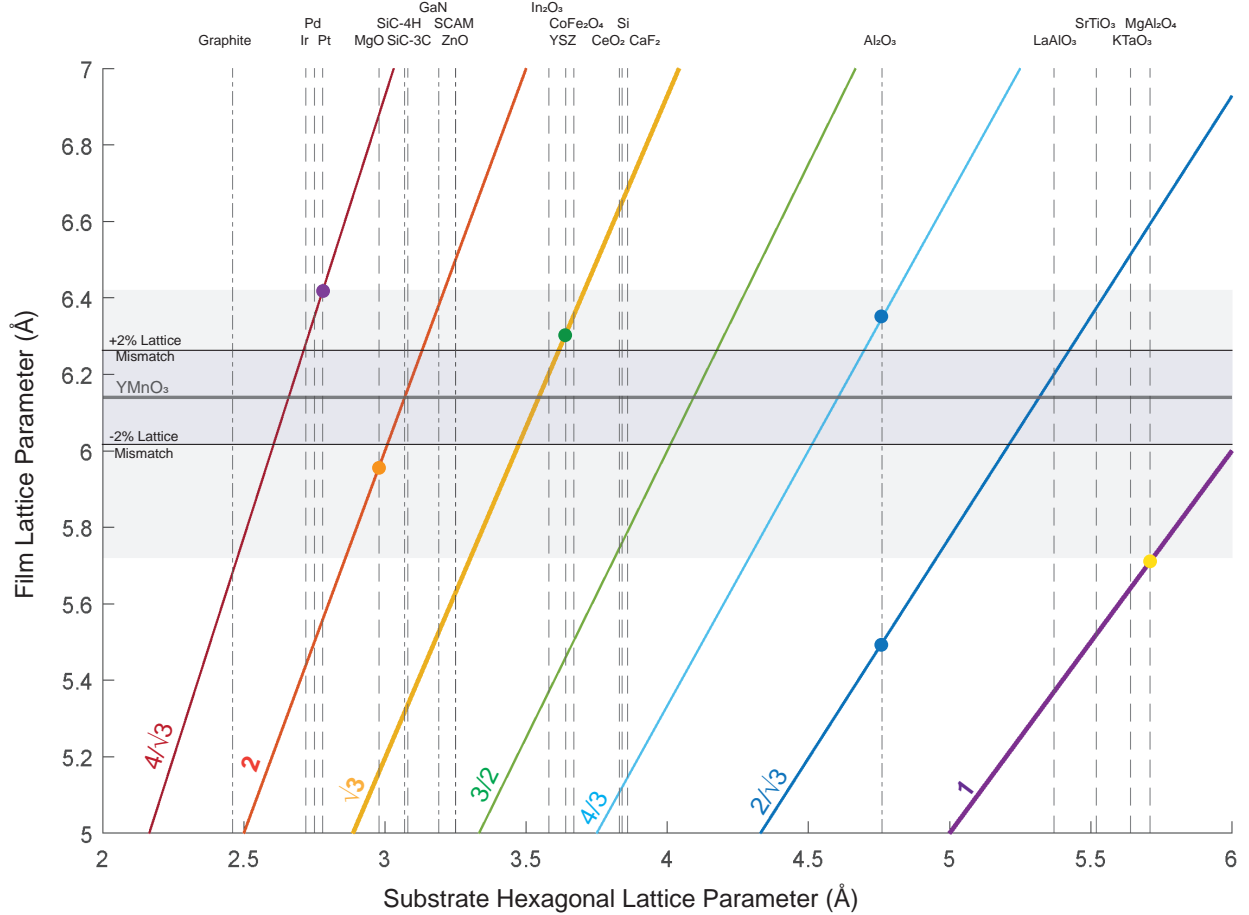


FIG. 9. In-plane lattice matching for hexagonal materials. Vertical lines indicate substrate (0001) (dot-dashed lines) and (111) (dashed lines) in-plane lattice parameters. The intersection between a vertical line and scaling factor indicates a possible effective substrate lattice parameter. The horizontal line at 6.14 Å represents YMnO₃ and the boundaries for $\pm 2\%$ lattice mismatch are labelled. The grey region indicates typical hexagonal film lattice parameters. Colored dots correspond to the lattice matching diagrams in Fig. 8. The thickness of the scaling factor lines roughly matches their likelihood of being realized, with 1 and $\sqrt{3}$ the most common.

IV. EPITAXY OF BULK-STABLE COMPOUNDS

Epitaxial thin-film synthesis of hexagonal ABO_3 materials was first achieved for the prototypical family of hexagonal rare-earth manganites ($RMnO_3$). In particular, initial focus centered on epitaxy of YMnO₃ as a model system for this materials class and YMnO₃ remains the most intensely studied member of hexagonal ABO_3 materials. The first attempts at epi-

taxial synthesis of hexagonal YMnO₃ in 1996 were motivated by its high-temperature uniaxial ferroelectricity combined with its suitability for integration with silicon as non-volatile ferroelectric memories⁶⁰. Following the demonstration of magnetoelectric coupling effects in hexagonal RMnO₃ bulk crystals^{11,12}, interest shifted towards thin-film manifestation of such multiferroic properties and potential magnetoelectric effects. In 2006, Laukhin et al. demonstrated electrical control of magnetism in a permalloy/YMnO₃ thin-film heterostructure⁶¹, see Fig. 10(a). A giant flexoelectric effect was further observed in strained HoMnO₃ films⁶², which could be used to tune the ferroelectric properties (Fig. 10(b)). The discovery of the topologically protected vortex domain patterns in bulk crystal RMnO₃ compounds in 2010^{19,63} and subsequently their related domain-wall functionalities^{20,21}, sparked a renewed interest in the multiferroic domain structure and thickness scaling in hexagonal RMnO₃ thin films. Furthermore, the improper nature of the ferroelectric order in hexagonal ABO₃ oxides, which is driven by a non-ferroelectric structural distortion, suggests novel avenues for stabilizing and controlling spontaneous ferroelectric polarization in the ultrathin limit^{49,64}.

To date, the hexagonal phase has been realized as thin films for the entire bulk-stable rare-earth manganite series ($R = \text{Dy-Lu}$,^{38,60,65–71}) where epitaxial stabilization additionally extended the series to lighter rare-earth ions down to samarium (Sm-Tb,^{66,72–74}) that normally would crystallize in the orthorhombic $Pnma$ phase as further discussed in Sec. V. Here, hexagonal SmMnO₃ has been achieved only on an isostructural YMnO₃ substrate⁷², whereas the other members can be grown epitaxially on commercially available substrates such as YSZ(111). In addition to the rare-earth series and yttrium, the A -site of hexagonal manganites can accommodate both scandium and indium. However, to our knowledge, only the (epitaxially stabilized) orthorhombic phase of ScMnO₃ has been reported in thin films; growth of hexagonal InMnO₃ remains limited to polycrystalline films reported in the literature⁷⁵. In bulk InMnO₃, carefully tuning the defect chemistry or the thermal history of the crystals allows realizing trimerized domains of either $P6_3cm$ symmetry (see Fig. 1(d)), just as in the other rare-earth manganites, or domains of the anti-polar $P\bar{3}c1$ symmetry (Fig. 1(e)) seen at the domain walls between the polar trimerization domains in RMnO₃, all the while retaining the vortex domain pattern^{76–78}. Epitaxial realization of single-crystalline hexagonal InMnO₃ thus provides an interesting opportunity for studying the thin-film manifestation of these complementary symmetry properties.

As mentioned in Sec. III, a major challenge in thin-film growth of the hexagonal mangan-

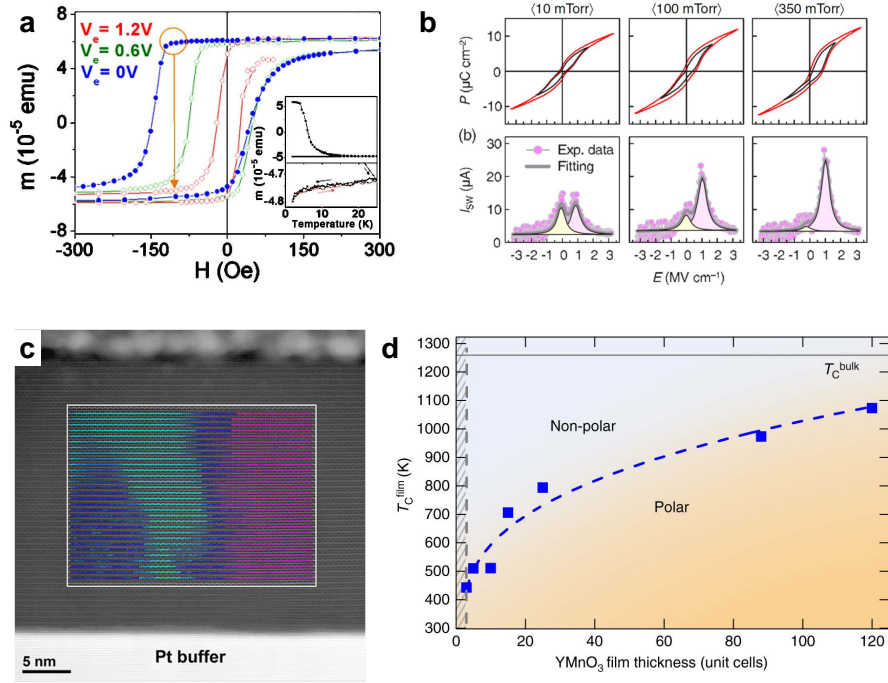


FIG. 10. Ferroelectric properties of hexagonal $RMnO_3$ thin films. (a) Voltage control of exchange bias in a permalloy layer through interfacial magnetic exchange in epitaxial multiferroic $YMnO_3$ grown on $Pt(111)/SrTiO_3(111)$. Reprinted figure with permission from Laukin *et al.* Phys. Rev. Lett. **97**, 227201 (2006). Copyright (2006) by the American Physical Society.⁶¹ (b) Modification of ferroelectric hysteresis loops in hexagonal $HoMnO_3$ films on $Pt(111)/Al_2O_3(0001)$ caused by the strain-gradient-induced flexoelectric effect. Reprinted figure with permission from Lee, D *et al.* Phys. Rev. Lett. **107**, 057602 (2011). Copyright (2011) by the American Physical Society.⁶² (c) Improper ferroelectric domain pattern mapped at the atomic scale in hexagonal $YMnO_3$ on $Pt(111)/YSZ(111)$ using HAADF-STEM. Each color represents one of six total trimerization domain states, with polarization pointing either up or down. (d) Improper ferroelectric transition temperatures in hexagonal $YMnO_3$ films grown on $YSZ(111)$ as function of film thickness. (c) and (d) reprinted from Nordlander *et al.* Nat. Commun. **10**, 5591 (2019). Copyright 2019 The Authors, licensed under a CC BY 4.0 license.⁴⁹

ites is the lack of isostructural or lattice-matching substrates. Added to this is a tendency to form crystallographic domains and defects due to close lattice matching between multiple crystallographic orientations of the hexagonal $RMnO_3$ structure and with the correspond-

ing binary oxide R_2O_3 ⁷⁹. Indeed, the higher symmetry of cubic substrates such as YSZ, compared to that of the layered hexagonal ABO_3 phase, impedes nucleation of a completely single-domain crystalline film and can cause defects such as antiphase boundaries. Thus, careful attention to substrate surface termination may play an important role in reducing the occurrence of these types of defects⁸⁰. The epitaxial quality of $RMnO_3$ films is also strongly dependent on substrate temperature during deposition. The hexagonal phase crystallizes down to 690°C⁸¹, however the highest crystalline quality is achieved in the range 750°C-900°C. Although hexagonal manganite thin films have been grown on a range of substrates including YSZ(111), Si(111), Pt(111), MgO(111), GaN(0001), ZnO(0001) and *c*-cut Al_2O_3 ^{60,61,65,70,82-87}, resulting in various degrees of crystallinity, not nearly as many options are commercially available as for their perovskite ABO_3 counterparts.

Over the past decade, significant improvement of the thin-film crystalline quality of $RMnO_3$ has been achieved and epitaxial layer-by-layer thin-film growth with sub-unit-cell thickness precision has recently been demonstrated⁸⁰. Such improvement of structural quality has been crucial to the investigation into the ultrathin manifestation of improper ferroelectric properties and domain structure^{49,74,88,89} in this class of materials (Fig. 10(c)). In particular, the structural distortion transforming the non-polar $P6_3/mmc$ phase to the polar $P6_3cm$ phase, and leading to the secondary ferroelectric polarization, was shown to be significantly modified by substrate-interface proximity, as demonstrated by a combination of in-situ high-angle annular dark-field scanning transmission electron microscopy (HAADF-STEM) and optical second harmonic generation (SHG)⁴⁹. The resulting threshold thickness for room-temperature polarization in $YMnO_3$ on an insulating substrate was determined to be two unit cells (Fig. 10(d)).

In hexagonal $RMnO_3$, the improper ferroelectric order coexists with antiferromagnetic order on the Mn^{3+} sublattice below 70-120 K, leading to multiferroicity. Because of the fully compensated nature of this antiferromagnetic order (i.e. lack of net magnetic moment), its thin-film manifestation has been challenging to study⁹⁰. Although neutron diffraction on thicker films of $YMnO_3$ (thickness exceeding 400 nm) shows Néel temperatures that closely match the bulk values⁶⁸, similar neutron measurements on thinner films are precluded due to the limited thin-film volume. Moreover, SQUID magnetometry has revealed spin-glass states in oxygen-deficient $YMnO_3$ films, indicating the strong influence of oxygen off-stoichiometry on the magnetic order^{69,91}. Hence, further work is needed to fully characterize

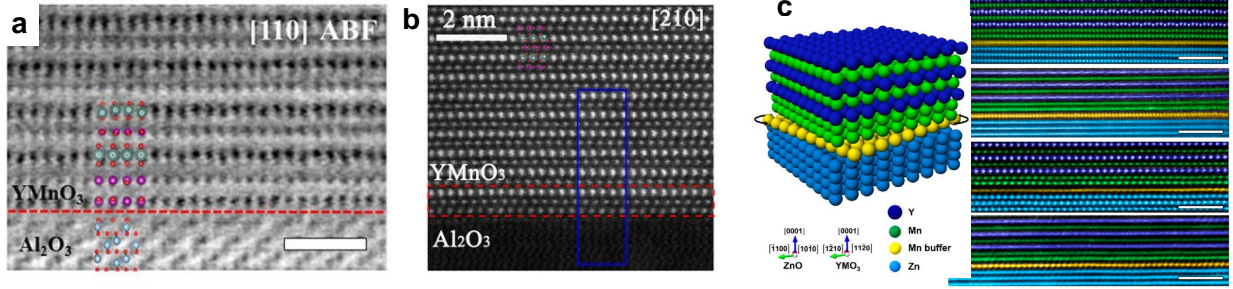


FIG. 11. Substrate–film interface reconstruction in hexagonal YMnO_3 thin films visualized by HAADF-STEM. (a), (b) Hexagonal YMnO_3 films on sapphire substrates exhibit a double Mn-O layer at the interface that can host a charge ordered state of Mn^{3+} and Mn^{2+} ions. Reprinted from Cheng *et al.* *Sci. Adv.* **4**, eaar4298 (2018). Copyright 2018 The Authors, some rights reserved; exclusive licensee AAAS. Distributed under a CC BY-NC 4.0 license.⁸⁷ (c) A triple Mn-O layer is formed between hexagonal YMnO_3 and a Zn-terminated $\text{ZnO}(0001)$ substrate. The Mn-O layer closest to the substrate is reported to adopt a 5° in-plane rotation relative to both film and substrate, influencing the strain relaxation of the YMnO_3 film. Reprinted with permission from Zhang *et al.* *Nano Lett.* **21**, 6867-6874 (2021). Copyright (2021) American Chemical Society.⁹⁴

the intrinsic magnetic state of ultrathin hexagonal RMnO_3 . Additionally, it is expected that the antiferromagnetic domain size is significantly reduced in thin films compared with bulk crystals, hampering real-space characterization⁹². Thus, the enigmatic multiferroic coupling of ferroelectric and antiferromagnetic domain patterns observed in RMnO_3 bulk crystals^{11,93} remains a topic for future investigations in RMnO_3 thin films.

In addition to dimensionality scaling and heterostructure integration, thin-film realization of quantum oxide materials offers the opportunity to use epitaxial constraints to further tune their functionality. The lattice mismatch with respect to the substrate can impart epitaxial strain in the thin film, or induce interface defects, that affect both electronic and magnetic properties. In hexagonal RMnO_3 , strain engineering can in principle be used to tune the improper ferroelectricity in terms of both domain configuration and polarization magnitude^{95–97}. Although thin-film RMnO_3 is often grown on substrates with large lattice mismatch exceeding 2% (see Fig. 9), the resulting epitaxial strain is not obvious⁹⁸. Rather than inducing a coherently strained thin-film lattice, several other mechanisms are often at play that accommodate this mismatch. For example, misfit dislocations are frequently seen

at the substrate–film interface, allowing bulk-like lattice constants to persist in the thin-film limit⁴⁹. Structural or chemical mismatch at interfaces can additionally be accommodated through oxygen off-stoichiometry⁶², in-plane lattice rotation⁹⁴, or interface reconstruction⁸⁷, as shown in Fig. 11. It is possible that coherently strained epitaxial films could be achieved in hexagonal $RMnO_3$ films if grown on substrates with smaller lattice mismatch. This, however, would require the design and development of new substrates that offer a better compatibility with the family of hexagonal ABO_3 materials.

An alternative route to achieve coherently strained heterostructures is demonstrated through the recent realization of mutual lattice matching between $RMnO_3$ and In_2O_3 -based transparent conducting layers such as indium-tin oxide (ITO). Straining the conducting layer to the $RMnO_3$ lattice⁸⁰, rather than vice versa, offers a new opportunity for epitaxial integration of hexagonal ABO_3 into functional oxide-electronic heterostructures and superlattices (Fig. 12(a)-(c)).

The layered structure of hexagonal ABO_3 further distinguishes this class of oxides as prospective quantum materials. As already seen in Sec. I, the triangular sub-lattice of each half-unit-cell layer breaks inversion symmetry (see Fig. 1(b)). Given the half-unit-cell layer-by-layer growth mode achieved by PLD⁸⁰, the symmetry of the ultrathin thin-film system can be alternately controlled between preserved and broken inversion symmetry, purely based on either an even or odd total number of half-unit-cell layers⁹⁹. This effect was demonstrated using in-situ SHG^{100,101} during hexagonal $RMnO_3$ epitaxial growth, where the emission of frequency-doubled light was turned on and off in the films by the deposition of each monolayer (Fig. 12(d)). Similar to 2D-layered van-der-Waals materials¹⁰², such a layer-dependent symmetry control in thin films could furthermore be used to not only tune nonlinear optical responses, but also may present an avenue to engineer, e.g., magnetoelectric, nonreciprocal, chiral or topological effects in the general class of hexagonal ABO_3 and their heterostructures.

Beyond the hexagonal manganites, the polar hexagonal $P6_3cm$ phase has been achieved as bulk crystals for certain gallates ($AGaO_3$, $A = Y, Er, Ho$ ¹⁰³) and indates ($AInO_3$, $A = Y, Sm-Ho$,^{104,105}) and the non-polar $P6_3/mmc$ hexagonal structure is the bulk-stable phase of $InFeO_3$ ^{106,107}. Although thin films of hexagonal gallates and indates remain little explored so far, thin films of $InFeO_3$ have been grown by PLD on both $ZnO(0001)$ and $Ta:SnO_2$ -buffered Al_2O_3 substrates^{44,108}. $InFeO_3$ films have been proposed as candidates for

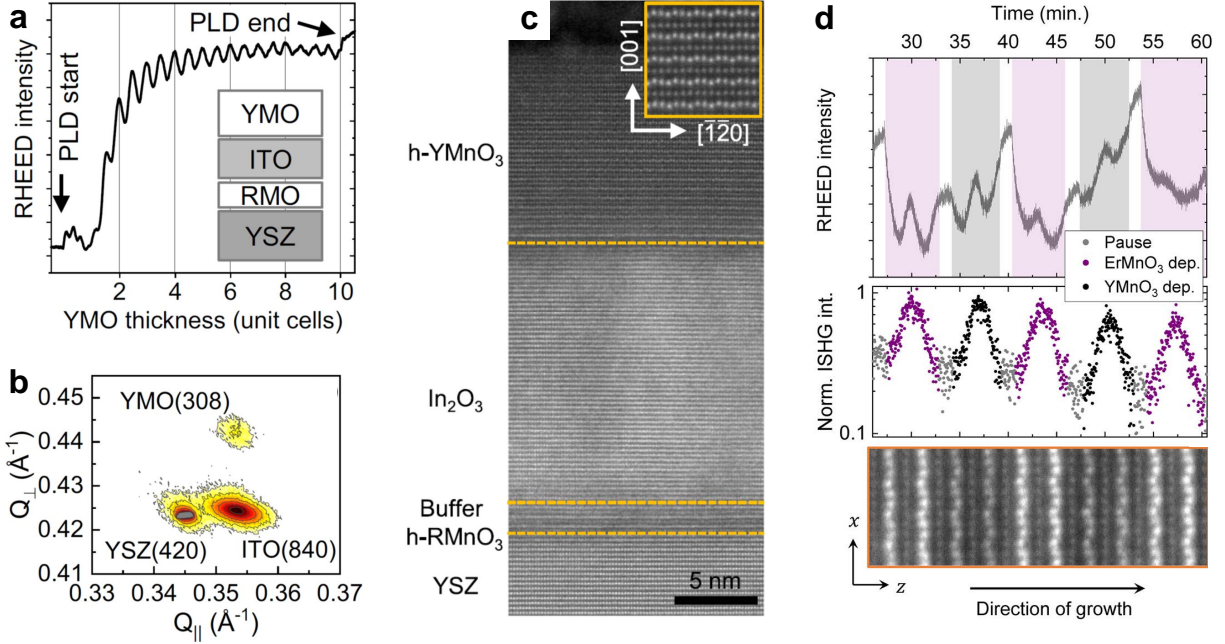


FIG. 12. Hexagonal $RMnO_3$ in epitaxial heterostructures. (a)-(c) Mutual lattice matching is achieved between $YMnO_3$ and indium tin oxide ($SnO_2:In_2O_3$, ITO) by inserting a buffer hexagonal $RMnO_3$ layer at the substrate interface to induce immediate strain relaxation. (a) RHEED oscillations indicating a layer-by-layer growth mode of $YMnO_3$ in this heterostructure. (b) X-ray reciprocal space mapping shows matching of in-plane lattice parameters between ITO and $YMnO_3$, yet relaxed compared to the underlying YSZ substrate. (c) HAADF-STEM image of a similar heterostructure. (a)-(c) Reprinted figures with permission from Nordlander *et al.* Phys. Rev. Lett. **4**, 124403 (2020). Copyright (2020) by the American Physical Society.⁸⁰ (d) A $(YMnO_3)_1/(ErMnO_3)_1$ superlattice grown on YSZ(111). In-situ optical second harmonic generation reveals the inversion-symmetry breaking of each half-unit-cell layer. Reprinted with permission from Nordlander *et al.* Nano Lett. **21**, 2780-2785 (2021). Copyright (2021) American Chemical Society.⁹⁹

watersplitting and photoelectrode applications due to their beneficial band-gap placement⁴⁴. Additionally, epitaxial $InFeO_3$ has been used as structurally compatible non-polar spacers in hexagonal $LuFeO_3$ -based superlattices grown by oxide MBE¹⁰⁹. The high volatility of indium and its sub-oxides¹¹⁰ at the elevated temperatures required for crystallization of the hexagonal phase, however, renders the thin-film synthesis of the indium-based hexagonal compounds challenging; such challenges can also be expected for hexagonal gallates given the similar volatility of gallium.

We note, however, that epitaxy of indates and gallates offers interesting opportunities to study the thin-film functional properties of hexagonal oxides in absence of transition metal ions and magnetism on the B site. This enables, for example, isolating the physics of frustrated rare-earth magnetism on the hexagonal A -site lattice³³. Moreover, in contrast to the transition-metal-based hexagonal ABO_3 oxides, which are mixed electronic and ionic conductors, the indates and gallates are electronically insulating and could thus support pure oxygen-ion conductivity.

V. EPITAXY OF METASTABLE HEXAGONAL ABO_3 COMPOUNDS

Thin film epitaxy is also a powerful platform for exploring metastable hexagonal oxides. During crystal growth, the phase that is deposited minimizes the global energy of the system. The Gibbs free energy of formation for a crystal nucleating on a substrate is comprised of a volume term, which will prefer the thermodynamically stable structure; a surface term, which is determined by the surface energy between the material and the substrate; and a stress term, which discourages the growth of highly stressed states. In the early stages of growth, the crystal nucleating on the substrate has a high surface-to-volume ratio, making the interface between the substrate and nucleating crystal a critical component in film growth. Because coherent crystalline interfaces require less energy to form than non-coherent ones, the film often adopts a structure which resembles the crystallographic structure of the substrate in epitaxial thin film growth. One of the powerful consequences of this minimization of interfacial energy between the substrate and film – known as epitaxial stabilization – is that a metastable crystal structure, not the lowest energy structure, can be grown^{111,112}. By careful choice of substrate^{58,113}, epitaxial stabilization enables the exploration of compounds in their metastable and non-equilibrium structures, opening the door to novel materials with new functionalities.

In the case of rare-earth manganites, $RMnO_3$, the ground-state structure depends largely on the R -site radius, as discussed in Sec. II. As the radius of the R -cation is decreased, the lower energy structure goes from orthorhombic (La – Dy) to hexagonal (Ho – Lu). The small energy difference in the bulk stable state near the crossover between orthorhombic and hexagonal (Fig. 6) can be overcome by epitaxial stabilization. For example, Bosak et al. demonstrated that EuMnO_3 , GdMnO_3 , and DyMnO_3 could form the hexagonal phase

by epitaxial stabilization on YSZ (111)⁶⁶, and that HoMnO₃, TmMnO₃ and LuMnO₃ could form the orthorhombic phase using LaAlO₃ (001) or SrTiO₃ (001) substrates¹¹⁴ (Table II).

Notably, unlike the manganites, there are no known bulk-stable hexagonal ferrites besides InFeO₃^{106,107}. Instead, the *R*FeO₃ ferrites are usually orthorhombic in their ground state, due to the crystal field splitting of the orbitals as discussed in section II. However, many of the *R*FeO₃ structures have been epitaxially stabilized for *R* with smaller cation radius (Y, Sc, Eu, Tb – Lu), as summarized in Table II. In addition to epitaxial stabilization, “stromataxic stabilization” can be used to further increase the number of compounds which can be synthesized in the thin film form⁵¹. Garten et al. showed that by using sequential atomic layering they could form hexagonal ScFeO₃ with the YMnO₃-like structure. In the same growth conditions, co-deposition of scandium and iron yielded the bixbyite polymorph. Stromataxic stabilization is a powerful technique that could likely be used to construct other metastable hexagonal oxides, beyond those which can be constructed by epitaxial stabilization alone.

Stabilizing these hexagonal *A*FeO₃ ferrites opens the door to further engineering their ferroelectric, magnetic, and multiferroic properties. Here we will focus on LuFeO₃, since it has seen a recent surge in interest – for an overview of the other *A*FeO₃ compositions, refer to an earlier review of hexagonal ferrites¹³⁰. While LuFeO₃ is stable in the orthorhombic structure in the bulk, it can be epitaxially stabilized to be isostructural to YMnO₃¹²¹, as shown in Table II. In addition to YSZ^{121,131}, LuFeO₃ has been epitaxially stabilized on the basal plane of Al₂O₃¹⁶, Ir(111), Pt(111)¹³², Fe₃O₄(111)¹²⁵, Sn:In₂O₃¹³³, and GaN¹³⁴. Figure 13a,b show high-resolution HAADF-STEM images of epitaxially stabilized LuFeO₃ synthesized by MOCVD (Fig. 13(a)) and MBE (Fig. 13(b)). This hexagonal structure is an improper ferroelectric with P6₃cm symmetry (similar to what was discussed in the previous section IV) with a polarization of 6.5 μC/cm²¹³² and a Curie Temperature around 1020 K¹⁶. The switching of the polarization by piezoforce microscopy¹⁵ is shown in Fig. 13(c). The hexagonal symmetry of the structure produces a frustrated system, that results in two-dimensional arrangements of spins in the iron planes, as shown in Fig. 2, resulting in an antiferromagnet. Below approximately 145 K, the spins cant in the [0001] direction, producing a net magnetic moment, displayed in Fig. 13(d)^{16,131}.

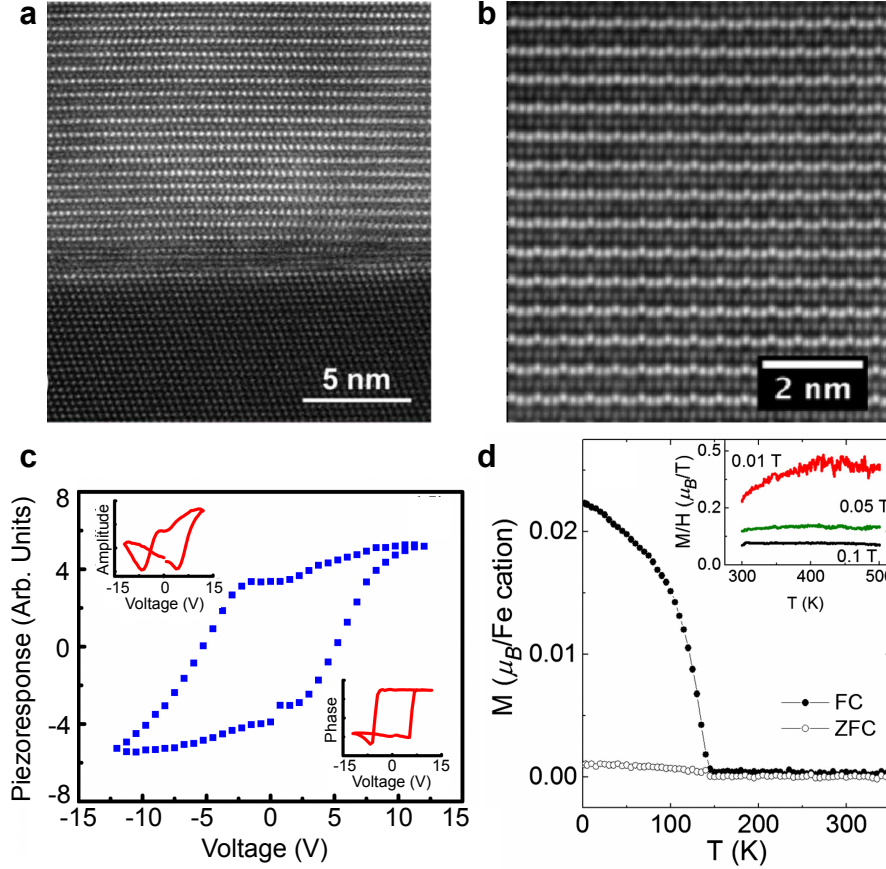


FIG. 13. Characterization of epitaxially-stabilized LuFeO_3 thin films. (a) HAADF STEM micrograph of a LuFeO_3 thin film on YSZ (111). Republished with permission from Akbashev *et al.* CrystEngComm. **14**, 5373-5376 (2012); permission conveyed through Copyright Clearance Center, Inc. Copyright 2012 The Royal Society of Chemistry.¹³⁵ (b) HAADF STEM micrograph showing the trimerization of the brighter lutetium atoms characteristic of the $P6_3cm$ structure. (c) PFM measurement of $\text{LuFeO}_3/\text{Pt}/\text{Al}_2\text{O}_3$ showing a hysteresis loop with phase and amplitude curves inset. Reprinted figure with permission from Wang *et al.* Phys. Rev. Lett. **110**, 237601 (2013). Copyright (2013) by the American Physical Society.¹⁵ (d) Magnetization vs. temperature in an 0.01 T field applied out of plane of a 250 nm film of LuFeO_3 on YSZ (111) indicating an weak AFM transition at 143 K with inset high temperature behavior at various applied fields. (b) and (d) Reprinted with permission from Disseler *et al.* Phys. Rev. Lett. **114**, 217602 (2015). Copyright (2015) by the American Physical Society.¹⁶

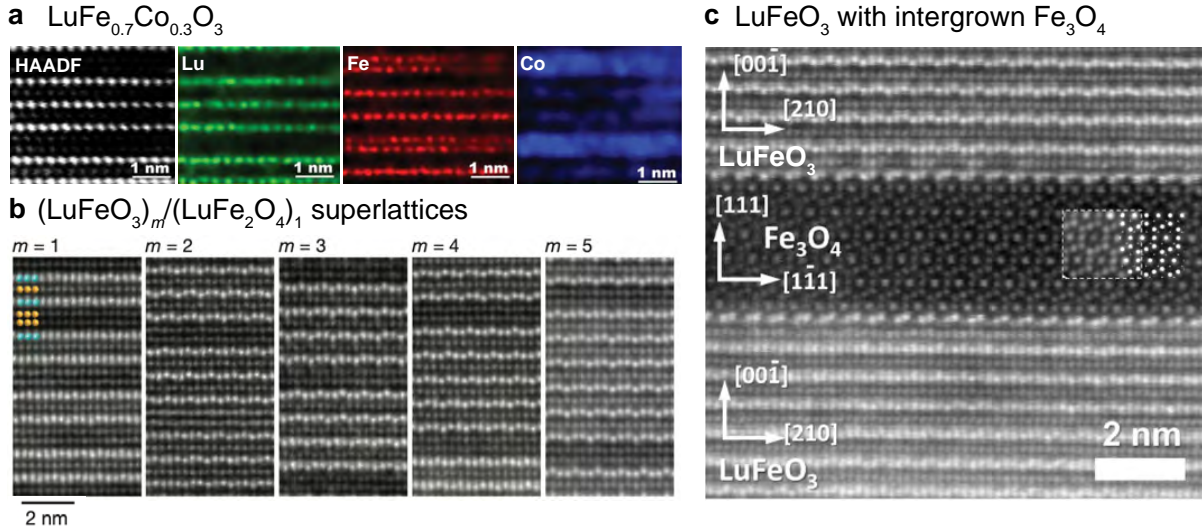


FIG. 14. STEM micrographs of LuFeO_3 thin films combined with other materials. (a) HAADF STEM and atomic resolution EDS of a small region of cobalt-doped LuFeO_3 , nominally $\text{LuFe}_{0.7}\text{Co}_{0.3}\text{O}_3$. Republished with permission from Akbashev *et al.* CrystEngComm. **14**, 5373-5376 (2012); permission conveyed through Copyright Clearance Center, Inc. Copyright 2012 The Royal Society of Chemistry.¹³⁵ (b) HAADF-STEM micrographs of the $m = 1-5$ members of the $(\text{LuFeO}_3)_m/(\text{LuFe}_2\text{O}_4)_1$ superlattice series imaged along the LuFeO_3 $[100]$ zone axis. The leftmost image shows the position of lutetium (teal) and iron (yellow) atomic columns. Reprinted by permission from Springer Nature Customer Service Centre GmbH: Mundy *et al.* Nature **537**, 523-527 (2016). Copyright 2016 Springer Nature.⁵⁰ (c) HAADF-STEM micrograph of an iron-rich LuFeO_3 film with ingrown epitaxial Fe_3O_4 nanolayers. Inset shows a HAADF-STEM simulation of Fe_3O_4 along with white dots that mark the imaged iron positions. Reprinted by permission from Springer Nature Customer Service Centre GmbH: Springer Nature; Akbashev, A *et al.* Sci. Rep. **2**, 672 (2012). Copyright 2012 The Authors.¹²⁵

Due to the simultaneous existence of ferroelectricity and a weak ferromagnetic moment, LuFeO_3 is a promising candidate for multiferroic materials. In particular, compared to the hexagonal manganites, the hexagonal ferrites promise higher magnetic transition temperatures and magnetoelectric coupling due to the additional occupied orbital¹⁷ (the five d electrons in Fe^{+3} half fill each of the orbitals in Fig. 5). While LuFeO_3 itself only has a net magnetic moment at cryogenic temperatures, LuFeO_3 can be synthesized in a superlattice with other materials in an effort to enhance the magnetism. The first attempts

included cobalt doped LuFeO_3 ¹³⁵, depicted in Fig. 14(a). It was found that these materials showed a decrease in the magnetic ordering temperatures with respect to LuFeO_3 and $\text{LuFe}_{2-x}\text{Co}_x\text{O}_4$. More recently, LuFeO_3 was grown in a superlattice structure with formula-unit-thick layers of LuFe_2O_4 , a hexagonal ferrite with a 240 K ferrimagnetic transition temperature, to create a room-temperature multiferroic⁵⁰. In these superlattices shown in Fig. 14(b), the ferroelectric rumpling from the LuFeO_3 reduced the magnetic frustration in the LuFe_2O_4 , increasing the magnetic transition temperature to 281 K. The material further demonstrated electric field control of magnetism – creating a magnetoelectric multiferroic (Fig. 15). This opens doors to the new engineering of multiferroic materials based on these epitaxially stabilized, improper ferroelectrics. We further note that LuFeO_3 can be epitaxially stabilized on intergrown spinel Fe_3O_4 (magnetite)¹²⁵. The very high magnetic ordering temperature of Fe_3O_4 and other spinel compounds could provide a pathway to create a multiferroic with simultaneous transitions well above room-temperature.

In addition to their coupled electrical and magnetic order, hexagonal ferrites, just as the hexagonal manganites, host topological defects such as their ferroelectric domain walls and vortices where six ferroelectric domains come to a point. The superlattice construction of the $(\text{LuFeO}_3)_m / \text{LuFe}_2\text{O}_4$ provides an avenue to manipulate these topological textures in these hexagonal ferroelectrics¹⁰⁹. As the confinement of the ferroelectric layer is increased, the material goes from stabilizing charged domain walls with 3 and 5-fold fractional vortices, to having irregular domains with neutral domain walls. As the confinement approaches one monolayer of LuFeO_3 , the ferroelectricity is suppressed – reminiscent of the ferroelectric to paraelectric transition with temperature.

VI. OUTLOOK

The hexagonal ABO_3 materials are a rich class of quantum materials. In addition to the well-studied multiferroic in the hexagonal manganites, there has been recent interest in stabilizing the elusive quantum spin liquid³³ and predicted topological semimetal states⁴⁷ and unconventional superconductivity³⁶. Thin film epitaxy provides a powerful platform for both studying these materials at the fundamental limits⁴⁹ as well as potentially stabilizing new materials. More recent work has used precise chemical layering⁵¹ to access compounds that were not accessible with epitaxial stabilization alone. Combined thin film epitaxy

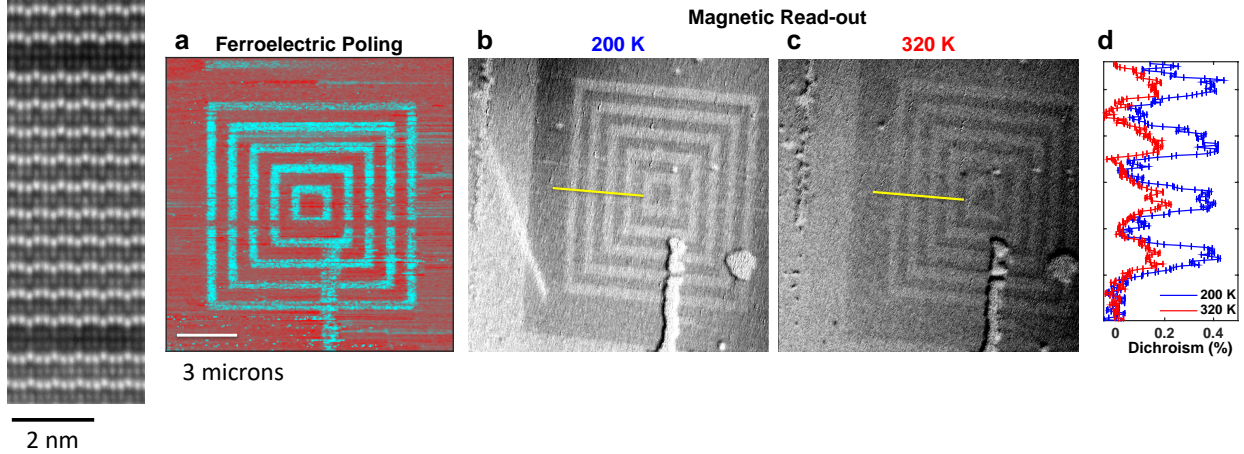


FIG. 15. Magneto-electric coupling in $(\text{LuFeO}_3)_m/\text{LuFe}_2\text{O}_4$ superlattices. Left, a HAADF STEM micrograph of a $(\text{LuFeO}_3)_9/\text{LuFe}_2\text{O}_4$ superlattice showing one period of the layered structure. (a) an out-of-plane PFM image at 300 K of an electrically poled region of the $m = 9$ superlattice film showing a pattern of up (teal) and down (red) c -axis polarized domains. (b) An XMCD PEEM image of the Fe L_3 edge of the poled region in (a) taken at 200 K. (c) The same image as (b) collected at 320 K. (d) Line profiles of the XMCD signal along the yellow lines in (b) and (c). The correspondance between the PFM and PEEM images demonstrates the coupling between improper ferroelectricity and ferrimagnetism in the film. Reprinted by permission from Springer Nature Customer Service Centre GmbH: Mundy *et al.* Nature **537**, 523-527 (2016). Copyright 2016 Springer Nature.⁵⁰

should allow additional emergent phenomena to be uncovered in the hexagonal oxides.

ACKNOWLEDGMENTS

The authors would like to thank Hena Das and EliseAnne Koskelo for fruitful discussions. This work is supported by the Air Force Research Laboratory, Project Grant FA95502110429. J.A.M acknowledges support from the Packard Foundation and Gordon and Betty Moore Foundation's EPiQS Initiative, Grant GBMF6760. J.N. acknowledges support from the Swiss National Science Foundation under Project No. P2EZP2_195686.

REFERENCES

- ¹H. Y. Hwang, Y. Iwasa, M. Kawasaki, B. Keimer, N. Nagaosa, and Y. Tokura, “Emergent phenomena at oxide interfaces,” *Nature Materials* **11**, 103–113 (2012).
- ²D. G. Schlom, L.-Q. Chen, X. Pan, A. Schmehl, and M. A. Zurbuchen, “A thin film approach to engineering functionality into oxides,” *Journal of the American Ceramic Society* **91**, 2429–2454 (2008).
- ³J. Mannhart and D. G. Schlom, “Oxide interfaces—an opportunity for electronics,” *Science* **327**, 1607–1611 (2010).
- ⁴L. T. Nguyen and R. Cava, “Hexagonal perovskites as quantum materials,” *Chemical Reviews* **121**, 2935–2965 (2020).
- ⁵H. Yakel, W. Koehler, E. Bertaut, and E. Forrat, “On the crystal structure of the manganese (iii) trioxides of the heavy lanthanides and yttrium,” *Acta Crystallographica* **16**, 957–962 (1963).
- ⁶M. Liliensblum, T. Lottermoser, S. Manz, S. M. Selbach, A. Cano, and M. Fiebig, “Ferroelectricity in the multiferroic hexagonal manganites,” *Nature Physics* **11**, 1070–1073 (2015).
- ⁷B. B. Van Aken, T. T. Palstra, A. Filippetti, and N. A. Spaldin, “The origin of ferroelectricity in magnetoelectric YMnO_3 ,” *Nature Materials* **3**, 164–170 (2004).
- ⁸C. J. Fennie and K. M. Rabe, “Ferroelectric transition in YMnO_3 from first principles,” *Physical Review B* **72**, 100103 (2005).
- ⁹E. Bertaut, R. Pauthenet, and M. Mercier, “Magnetic properties and structures of yttrium manganite,” *Physics Letters* **7**, 110–111 (1963).
- ¹⁰Z. J. Huang, Y. Cao, Y. Y. Sun, Y. Y. Xue, and C. W. Chu, “Coupling between the ferroelectric and antiferromagnetic orders in YMnO_3 ,” *Physical Review B* **56**, 2623–2626 (1997).
- ¹¹M. Fiebig, T. Lottermoser, D. Fröhlich, A. V. Goltsev, and R. V. Pisarev, “Observation of coupled magnetic and electric domains,” *Nature* **419**, 818–820 (2002).
- ¹²T. Lottermoser, T. Lonkai, U. Amann, D. Hohlwein, J. Ihringer, and M. Fiebig, “Magnetic phase control by an electric field,” *Nature* **430**, 541–544 (2004).
- ¹³B. Lorenz, “Hexagonal Manganites—(RMnO_3): Class (I) Multiferroics with Strong Coupling of Magnetism and Ferroelectricity,” *ISRN Condensed Matter Physics* **2013**, 497073

(2013).

- ¹⁴A. Akbashev, A. Semisalova, N. Perov, and A. Kaul, “Weak ferromagnetism in hexagonal orthoferrites $R\text{FeO}_3$ ($R = \text{Lu}, \text{Er-Tb}$),” *Applied Physics Letters* **99**, 122502 (2011).
- ¹⁵W. Wang, J. Zhao, W. Wang, Z. Gai, N. Balke, M. Chi, H. N. Lee, W. Tian, L. Zhu, X. Cheng, D. J. Keavney, J. Yi, T. Z. Ward, P. C. Snijders, H. M. Christen, W. Wu, J. Shen, and X. Xu, “Room-temperature multiferroic hexagonal LuFeO_3 films,” *Physical Review Letters* **110**, 237601 (2013).
- ¹⁶S. M. Disseler, J. A. Borchers, C. M. Brooks, J. A. Mundy, J. A. Moyer, D. A. Hillsberry, E. L. Thies, D. A. Tenne, J. Heron, M. E. Holtz, J. D. Clarkson, G. M. Stiehl, P. Schiffer, D. A. Muller, D. G. Schlom, and W. D. Ratchiff, “Magnetic structure and ordering of multiferroic hexagonal LuFeO_3 ,” *Physical Review Letters* **114**, 217602 (2015).
- ¹⁷H. Das, A. L. Wysocki, Y. Geng, W. Wu, and C. J. Fennie, “Bulk magnetoelectricity in the hexagonal manganites and ferrites,” *Nature Communications* **5**, 2998 (2014).
- ¹⁸S. Manipatruni, D. E. Nikonov, C.-C. Lin, T. A. Gosavi, H. Liu, B. Prasad, Y.-L. Huang, E. Bonturim, R. Ramesh, and I. A. Young, “Scalable energy-efficient magnetoelectric spin-orbit logic,” *Nature* **565**, 35–42 (2019).
- ¹⁹T. Choi, Y. Horibe, H. Yi, Y. J. Choi, W. Wu, and S.-W. Cheong, “Insulating interlocked ferroelectric and structural antiphase domain walls in multiferroic YMnO_3 ,” *Nature Materials* **9**, 253–258 (2010).
- ²⁰D. Meier, J. Seidel, A. Cano, K. Delaney, Y. Kumagai, M. Mostovoy, N. A. Spaldin, R. Ramesh, and M. Fiebig, “Anisotropic conductance at improper ferroelectric domain walls,” *Nature Materials* **11**, 284–288 (2012).
- ²¹J. A. Mundy, J. Schaab, Y. Kumagai, A. Cano, M. Stengel, I. P. Krug, D. M. Gottlob, H. Doğanay, M. E. Holtz, R. Held, Z. Yan, E. Bourret, C. M. Schneider, D. G. Schlom, D. A. Muller, R. Ramesh, N. A. Spaldin, and D. Meier, “Functional electronic inversion layers at ferroelectric domain walls,” *Nature Materials* **16**, 622–627 (2017).
- ²²S. M. Griffin, M. Lilienblum, K. T. Delaney, Y. Kumagai, M. Fiebig, and N. A. Spaldin, “Scaling behavior and beyond equilibrium in the hexagonal manganites,” *Physical Review X* **2**, 041022 (2012).
- ²³S.-Z. Lin, X. Wang, Y. Kamiya, G.-W. Chern, F. Fan, D. Fan, B. Casas, Y. Liu, V. Kiryukhin, W. H. Zurek, C. D. Batista, and S.-W. Cheong, “Topological defects as relics of emergent continuous symmetry and higgs condensation of disorder in fer-

- roelectrics,” *Nature Physics* **10**, 970–977 (2014).
- ²⁴Q. N. Meier, M. Lilienblum, S. M. Griffin, K. Conder, E. Pomjakushina, Z. Yan, E. Bourret, D. Meier, F. Lichtenberg, E. K. H. Salje, N. A. Spaldin, M. Fiebig, and A. Cano, “Global formation of topological defects in the multiferroic hexagonal manganites,” *Physical Review X* **7**, 041014 (2017).
- ²⁵Q. N. Meier, A. Stucky, J. Teyssier, S. M. Griffin, D. van der Marel, and N. A. Spaldin, “Manifestation of structural higgs and goldstone modes in the hexagonal manganites,” *Physical Review B* **102**, 014102 (2020).
- ²⁶M. Norman, “Colloquium: Herbertsmithite and the search for the quantum spin liquid,” *Reviews of Modern Physics* **88**, 041002 (2016).
- ²⁷Y. Kasahara, T. Ohnishi, Y. Mizukami, O. Tanaka, S. Ma, K. Sugii, N. Kurita, H. Tanaka, J. Nasu, Y. Motome, T. Shibauchi, and Y. Matsuda, “Majorana quantization and half-integer thermal quantum hall effect in a kitaev spin liquid,” *Nature* **559**, 227–231 (2018).
- ²⁸V. Kataev, A. Möller, U. Löw, W. Jung, N. Schittner, M. Kriener, and A. Freimuth, “Structural and magnetic properties of the new low-dimensional spin magnet $\text{InCu}_{2/3}\text{V}_{1/3}\text{O}_3$,” *Journal of Magnetism and Magnetic Materials* **290**, 310–313 (2005).
- ²⁹Y. Yan, Z. Li, T. Zhang, X. Luo, G. Ye, Z. Xiang, P. Cheng, L.-J. Zou, and X. Chen, “Magnetic properties of the doped spin-1/2 honeycomb-lattice compound $\text{In}_3\text{Cu}_2\text{VO}_9$,” *Physical Review B* **85**, 085102 (2012).
- ³⁰D.-Y. Liu, Y. Guo, X.-L. Zhang, J.-L. Wang, Z. Zeng, H.-Q. Lin, and L.-J. Zou, “Interlayer magnetic-frustration-driven quantum spin disorder in the honeycomb compound $\text{In}_3\text{Cu}_2\text{VO}_9$,” *EPL (Europhysics Letters)* **103**, 47010 (2013).
- ³¹W. Wu, M. M. Scherer, C. Honerkamp, and K. Le Hur, “Correlated dirac particles and superconductivity on the honeycomb lattice,” *Physical Review B* **87**, 094521 (2013).
- ³²D. A. Vander Griend, S. Boudin, V. Caignaert, K. R. Poeppelmeier, Y. Wang, V. P. Dravid, M. Azuma, M. Takano, Z. Hu, and J. D. Jorgensen, “ $\text{La}_4\text{Cu}_3\text{MoO}_{12}$: A novel cuprate with unusual magnetism,” *Journal of the American Chemical Society* **121**, 4787–4792 (1999).
- ³³L. Clark, G. Sala, D. D. Maharaj, M. B. Stone, K. S. Knight, M. T. Telling, X. Wang, X. Xu, J. Kim, Y. Li, S.-W. Cheong, and B. D. Gaulin, “Two-dimensional spin liquid behaviour in the triangular-honeycomb antiferromagnet TbInO_3 ,” *Nature Physics* **15**, 262–268 (2019).

- ³⁴J. A. Mundy, Q. Mao, C. M. Brooks, D. G. Schlom, and D. A. Muller, “Atomic-resolution chemical imaging of oxygen local bonding environments by electron energy loss spectroscopy,” *Applied Physics Letters* **101**, 042907 (2012).
- ³⁵S. Remsen and B. Dabrowski, “Synthesis and oxygen storage capacities of hexagonal $\text{Dy}_{1-x}\text{Y}_x\text{MnO}_{3+\delta}$,” *Chemistry of Materials* **23**, 3818–3827 (2011).
- ³⁶J. Hu, C. Le, and X. Wu, “Predicting unconventional high-temperature superconductors in trigonal bipyramidal coordinations,” *Physical Review X* **5**, 041012 (2015).
- ³⁷X. Huang, T. R. Paudel, S. Dong, and E. Y. Tsymbal, “Hexagonal rare-earth manganites as promising photovoltaics and light polarizers,” *Physical Review B* **92**, 125201 (2015).
- ³⁸H. Han, S. Song, J. H. Lee, K. J. Kim, G. W. Kim, T. Park, and H. M. Jang, “Switchable Photovoltaic Effects in Hexagonal Manganite Thin Films Having Narrow Band Gaps,” *Chemistry of Materials* **27**, 7425–7432 (2015).
- ³⁹J. Li, A. W. Sleight, and M. Subramanian, “Determination of the local environment of Mn^{3+} and In^{3+} in the $\text{YInO}_3\text{–YMnO}_3$ solid solution, which exhibits an intense blue color,” *Chemistry of Materials* **28**, 6050–6053 (2016).
- ⁴⁰S. H. Skjærvø, E. T. Wefring, S. K. Nesdal, N. H. Gaukås, G. H. Olsen, J. Glaum, T. Tybell, and S. M. Selbach, “Interstitial oxygen as a source of p-type conductivity in hexagonal manganites,” *Nature Communications* **7**, 13745 (2016).
- ⁴¹J. Kasahara, T. Katayama, S. Mo, A. Chikamatsu, Y. Hamasaki, S. Yasui, M. Itoh, and T. Hasegawa, “Room-temperature antiferroelectricity in multiferroic hexagonal rare-earth ferrites,” *ACS Applied Materials & Interfaces* **13**, 4230–4235 (2021).
- ⁴²L. Wu, C. Y. Jimmy, L. Zhang, X. Wang, and S. Li, “Selective self-propagating combustion synthesis of hexagonal and orthorhombic nanocrystalline yttrium iron oxide,” *Journal of Solid State Chemistry* **177**, 3666–3674 (2004).
- ⁴³Y. Zhang, J. Yang, J. Xu, Q. Gao, and Z. Hong, “Controllable synthesis of hexagonal and orthorhombic YFeO_3 and their visible-light photocatalytic activities,” *Materials Letters* **81**, 1–4 (2012).
- ⁴⁴B. Zhang, M. Seki, H. Zhou, J. Chen, and H. Tabata, “ InFeO_3 photoelectrode with two-dimensional superlattice for visible- and ultraviolet-light-driven water splitting,” *APL Materials* **8**, 051107 (2020).
- ⁴⁵D. Choudhury, A. Hazarika, A. Venimadhav, C. Kakarla, K. T. Delaney, P. S. Devi, P. Mondal, R. Nirmala, J. Gopalakrishnan, N. A. Spaldin, U. V. Waghmare, and D. D.

- Sarma, “Electric and magnetic polarizabilities of hexagonal Ln_2CuTiO_6 ($Ln = Y, Dy, Ho, Er,$ and Yb),” *Physical Review B* **82**, 134203 (2010).
- ⁴⁶M. G. Kim, B. Winn, S. Chi, A. T. Savici, J. A. Rodriguez-Rivera, W. C. Chen, X. Xu, Y. Li, J. W. Kim, S.-W. Cheong, and V. Kiryukhin, “Spin-liquid-like state in pure and Mn-doped $TbInO_3$ with a nearly triangular lattice,” *Physical Review B* **100**, 024405 (2019).
- ⁴⁷S. F. Weber, S. M. Griffin, and J. B. Neaton, “Topological semimetal features in the multiferroic hexagonal manganites,” *Physical Review Materials* **3**, 064206 (2019).
- ⁴⁸C. Lu, L.-D. Zhang, X. Wu, F. Yang, and J. Hu, “ $d+id$ chiral superconductivity in a triangular lattice from trigonal bipyramidal complexes,” *Physical Review B* **97**, 165110 (2018).
- ⁴⁹J. Nordlander, M. Campanini, M. D. Rossell, R. Erni, Q. N. Meier, A. Cano, N. Spaldin, M. Fiebig, and M. Trassin, “The ultrathin limit of improper ferroelectricity,” *Nature Communications* **10**, 5591 (2019).
- ⁵⁰J. A. Mundy, C. M. Brooks, M. E. Holtz, J. A. Moyer, H. Das, A. F. Rébola, J. T. Heron, J. D. Clarkson, S. M. Disseler, Z. Liu, A. Farhan, R. Held, R. Hovden, E. Padgett, Q. Mao, H. Paik, R. Misra, L. F. Kourkoutis, E. Arenholz, A. Scholl, J. A. Borchers, W. D. Ratcliff, R. Ramesh, C. J. Fennie, P. Schiffer, D. A. Muller, and D. G. Schlom, “Atomically engineered ferroic layers yield a room-temperature magnetoelectric multiferroic,” *Nature* **537**, 523–527 (2016).
- ⁵¹L. M. Garten, Z. Jiang, H. Paik, J. D. Perkins, A. Kakekhani, R. Fei, D. J. Werder, M. E. Holtz, D. S. Ginley, A. M. Rappe, D. E. Schlom, and M. L. Staruch, “Stromataxic stabilization of a metastable layered $ScFeO_3$ polymorph,” *Chemistry of Materials* **33**, 7423–7431 (2021).
- ⁵²R. D. Shannon and C. T. Prewitt, “Revised values of effective ionic radii,” *Acta Crystallographica Section B: Structural Crystallography and Crystal Chemistry* **26**, 1046–1048 (1970).
- ⁵³R. I. Hines, *Atomistic simulation and ab initio studies of polar solids.*, Ph.D. thesis, University of Bristol (1997).
- ⁵⁴D. Reinen, “The jahn-teller effect in solid state chemistry of transition metal compounds,” *Journal of Solid State Chemistry* **27**, 71–85 (1979).

- ⁵⁵K. Kamata, T. Nakajima, and T. Nakamura, “Thermogravimetric study of rare earth manganites $AMnO_3$ ($A= Sm, Dy, Y, Er, Yb$) at $1200^\circ C$,” *Materials Research Bulletin* **14**, 1007–1012 (1979).
- ⁵⁶K.-H. Hellwege, “Landolt bornstein, numerical data and functional relationship in science and technology,” *Elastic, Piezoelectric, Pyroelectric, Piezooptic, Electrooptic Constants, and Nonlinear Dielectric Susceptibilities of Crystal* (1979).
- ⁵⁷K. Nagashio and K. Kuribayashi, “Metastable phase formation from an undercooled rare-earth orthoferrite melt,” *Journal of the American Ceramic Society* **85**, 2550–2556 (2002).
- ⁵⁸T. Katayama, Y. Hamasaki, S. Yasui, A. Miyahara, and M. Itoh, “Epitaxial thin film growth of garnet-, $GdFeO_3$ -, and $YMnO_3$ -type $LuFeO_3$ using pulsed laser deposition,” *Thin Solid Films* **642**, 41–44 (2017).
- ⁵⁹R. Uecker, R. Bertram, M. Brützmam, Z. Galazka, T. M. Gesing, C. Guguschev, D. Klimm, M. Klupsch, A. Kwasniewski, and D. G. Schlom, “Large-lattice-parameter perovskite single-crystal substrates,” *Journal of Crystal Growth* **457**, 137–142 (2017).
- ⁶⁰N. Fujimura, T. Ishida, T. Yoshimura, and T. Ito, “Epitaxially grown $YMnO_3$ film: New candidate for nonvolatile memory devices,” *Applied Physics Letters* **69**, 1011–1013 (1996).
- ⁶¹V. Laukhin, V. Skumryev, X. Martí, D. Hrabovsky, F. Sánchez, M. V. García-Cuenca, C. Ferrater, M. Varela, U. Lüders, J. F. Bobo, and J. Fontcuberta, “Electric-field control of exchange bias in multiferroic epitaxial heterostructures,” *Physical Review Letters* **97**, 227201 (2006).
- ⁶²D. Lee, A. Yoon, S. Y. Jang, J. G. Yoon, J. S. Chung, M. Kim, J. F. Scott, and T. W. Noh, “Giant flexoelectric effect in ferroelectric epitaxial thin films,” *Physical Review Letters* **107**, 057602 (2011).
- ⁶³T. Jungk, Á. Hoffmann, M. Fiebig, and E. Soergel, “Electrostatic topology of ferroelectric domains in $YMnO_3$,” *Applied Physics Letters* **97**, 12904 (2010).
- ⁶⁴N. Sai, C. J. Fennie, and A. A. Demkov, “Absence of critical thickness in an ultrathin improper ferroelectric film,” *Physical Review Letters* **102**, 107601 (2009).
- ⁶⁵J. Dho, C. W. Leung, J. L. MacManus-Driscoll, and M. G. Blamire, “Epitaxial and oriented $YMnO_3$ film growth by pulsed laser deposition,” *Journal of Crystal Growth* **267**, 548–553 (2004).
- ⁶⁶A. Bosak, C. Dubourdieu, J.-P. Sénateur, O. Y. Gorbenko, and A. Kaul, “Epitaxial stabilization of hexagonal $RMnO_3$ ($R= Eu-Dy$) manganites,” *Journal of Materials Chemistry*

- 12**, 800–801 (2002).
- ⁶⁷J.-W. Kim, L. Schultz, K. Dörr, B. B. Van Aken, and M. Fiebig, “Growth and multiferroic properties of hexagonal HoMnO₃ films,” *Applied Physics Letters* **90**, 012502 (2007).
- ⁶⁸I. Gélard, C. Dubourdieu, S. Pailhès, S. Petit, and C. Simon, “Neutron diffraction study of hexagonal manganite YMnO₃, HoMnO₃, and ErMnO₃ epitaxial films,” *Applied Physics Letters* **92**, 232506 (2008).
- ⁶⁹S. Y. Jang, D. Lee, J.-H. Lee, T. W. Noh, Y. Jo, M.-H. Jung, and J.-S. Chung, “Oxygen vacancy induced re-entrant spin glass behavior in multiferroic ErMnO₃ thin films,” *Applied Physics Letters* **93**, 162507 (2008).
- ⁷⁰A. Posadas, J.-B. Yau, and C. H. Ahn, “Epitaxial multiferroic hexagonal manganite thin films grown on ZnO,” *physica status solidi (b)* **243**, 2085–2088 (2006).
- ⁷¹T. Takahashi, T. Yoshimura, and N. Fujimura, “Growth and Ferromagnetic Properties of Ferroelectric YbMnO₃ Thin Films,” *Japanese Journal of Applied Physics* **45**, 7329–7331 (2006).
- ⁷²K. R. Balasubramaniam, S. Havelia, P. A. Salvador, H. Zheng, and J. F. Mitchell, “Epitaxial stabilization and structural properties of *REMnO₃* (*RE* = Dy, Gd, Sm) compounds in a layered, hexagonal *ABO₃* structure,” *Applied Physics Letters* **91**, 232901 (2007).
- ⁷³J.-H. Lee, P. Murugavel, H. Ryu, D. Lee, J. Y. Jo, J. W. Kim, H. J. Kim, K. H. Kim, Y. Jo, M.-H. Jung, Y. H. Oh, Y.-W. Kim, J.-G. Yoon, J.-S. Chung, and T. W. Noh, “Epitaxial stabilization of a new multiferroic hexagonal phase of TbMnO₃ thin films,” *Advanced Materials* **18**, 3125–3129 (2006).
- ⁷⁴R. Mandal, M. Hirsbrunner, V. Roddatis, R. Gruhl, L. Schüler, U. Roß, S. Merten, P. Gegenwart, and V. Moshnyaga, “Strain-driven structure-ferroelectricity relationship in hexagonal TbMnO₃ films,” *Physical Review B* **102**, 104106 (2020).
- ⁷⁵C. R. Serrao, S. B. Krupanidhi, J. Bhattacharjee, U. V. Waghmare, A. K. Kundu, and C. N. R. Rao, “InMnO₃: A biferroic,” *Journal of Applied Physics* **100**, 076104 (2006).
- ⁷⁶Y. Kumagai, A. A. Belik, M. Lilienblum, N. Leo, M. Fiebig, and N. A. Spaldin, “Observation of persistent centrosymmetry in the hexagonal manganite family,” *Physical Review B* **85**, 174422 (2012), arXiv:arXiv:1109.1448v2.
- ⁷⁷F. T. Huang, X. Wang, S. M. Griffin, Y. Kumagai, O. Gindele, M. W. Chu, Y. Horibe, N. A. Spaldin, and S. W. Cheong, “Duality of topological defects in hexagonal manganites,” *Physical Review Letters* **113**, 267602 (2014).

- ⁷⁸S. M. Griffin, M. Reidulff, S. M. Selbach, and N. A. Spaldin, “Defect chemistry as a crystal structure design parameter: Intrinsic point defects and Ga substitution in InMnO_3 ,” *Chemistry of Materials* **29**, 2425–2434 (2017).
- ⁷⁹N. Jehanathan, O. Lebedev, I. Gélard, C. Dubourdieu, and G. Van Tendeloo, “Structure and defect characterization of multiferroic ReMnO_3 films and multilayers by TEM,” *Nanotechnology* **21**, 075705 (2010).
- ⁸⁰J. Nordlander, M. D. Rossell, M. Campanini, M. Fiebig, and M. Trassin, “Epitaxial integration of improper ferroelectric hexagonal YMnO_3 thin films in heterostructures,” *Physical Review Materials* **4**, 124403 (2020).
- ⁸¹T. Choi and J. Lee, “Bi modification for low-temperature processing of YMnO_3 thin films,” *Applied Physics Letters* **84**, 5043–5045 (2004).
- ⁸²S. Imada, S. Shouriki, E. Tokumitsu, and H. Ishiwara, “Epitaxial Growth of Ferroelectric YMnO_3 Thin Films on Si (111) Substrates by Molecular Beam Epitaxy,” *Japanese Journal of Applied Physics* **37**, 6497–6501 (1998).
- ⁸³S. Imada, T. Kuraoka, E. Tokumitsu, and H. Ishiwara, “Ferroelectricity of YMnO_3 Thin Films on $\text{Pt}(111)/\text{Al}_2\text{O}_3$ (0001) and $\text{Pt}(111)/\text{Y}_2\text{O}_3$ (111)/ $\text{Si}(111)$ Structures Grown by Molecular Beam Epitaxy,” *Japanese Journal of Applied Physics* **40**, 666–671 (2001).
- ⁸⁴X. Martí, F. Sánchez, D. Hrabovsky, J. Fontcuberta, V. Laukhin, V. Skumryev, M. V. García-Cuenca, C. Ferrater, M. Varela, U. Lüders, J. F. Bobo, S. Estradé, J. Arbiol, and F. Peiró, “Epitaxial growth of biferroic $\text{YMnO}_3(0\ 0\ 0\ 1)$ on platinum electrodes,” *Journal of Crystal Growth* **299**, 288–294 (2007).
- ⁸⁵K. H. Wu, H.-J. Chen, Y. T. Chen, C. C. Hsieh, C. W. Luo, T. M. Uen, J. Y. Juang, J.-Y. Lin, T. Kobayashi, and M. Gospodinov, “Marked enhancement of Néel temperature in strained YMnO_3 thin films probed by femtosecond spectroscopy,” *EPL (Europhysics Letters)* **94**, 27006 (2011).
- ⁸⁶Y. Chye, T. Liu, D. Li, K. Lee, D. Lederman, and T. H. Myers, “Molecular beam epitaxy of YMnO_3 on *c*-plane GaN,” *Applied Physics Letters* **88**, 132903 (2006).
- ⁸⁷S. Cheng, C. Xu, S. Deng, M.-G. Han, S. Bao, J. Ma, C. Nan, W. Duan, L. Bellaiche, Y. Zhu, and J. Zhu, “Interface reconstruction with emerging charge ordering in hexagonal manganite,” *Science Advances* **4**, eaar4298 (2018).
- ⁸⁸H. Pang, F. Zhang, M. Zeng, X. Gao, M. Qin, X. Lu, J. Gao, J. Dai, and Q. Li, “Preparation of epitaxial hexagonal YMnO_3 thin films and observation of ferroelectric vortex

- domains,” *npj Quantum Materials* **1**, 16015 (2016).
- ⁸⁹D. J. Kim, J. G. Connell, S. S. A. Seo, and A. Gruverman, “Domain wall conductivity in semiconducting hexagonal ferroelectric TbMnO₃ thin films,” *Nanotechnology* **27**, 155705 (2016).
- ⁹⁰J. Fontcuberta, “Multiferroic RMnO₃ thin films,” *Comptes Rendus Physique* **16**, 204–226 (2015).
- ⁹¹S. Cheng, M. Li, S. Deng, S. Bao, P. Tang, W. Duan, J. Ma, C. Nan, and J. Zhu, “Manipulation of Magnetic Properties by Oxygen Vacancies in Multiferroic YMnO₃,” *Advanced Functional Materials* **26**, 3589–3598 (2016).
- ⁹²T. Kordel, C. Wehrenfennig, D. Meier, T. Lottermoser, M. Fiebig, I. Gélard, C. Dubourdieu, J. W. Kim, L. Schultz, and K. Dörr, “Nanodomains in multiferroic hexagonal RMnO₃ films ($R = Y, Dy, Ho, Er$),” *Physical Review B* **80**, 045409 (2009).
- ⁹³M. Giraldo, Q. N. Meier, A. Bortis, D. Nowak, N. A. Spaldin, M. Fiebig, M. C. Weber, and T. Lottermoser, “Magnetoelectric coupling of domains, domain walls and vortices in a multiferroic with independent magnetic and electric order,” *Nature Communications* **12**, 3093 (2021).
- ⁹⁴Y. Zhang, W. Si, Y. Jia, P. Yu, R. Yu, and J. Zhu, “Controlling strain relaxation by interface design in highly lattice-mismatched heterostructure,” *Nano Letters* **21**, 6867–6874 (2021).
- ⁹⁵S. Artyukhin, K. T. Delaney, N. A. Spaldin, and M. Mostovoy, “Landau theory of topological defects in multiferroic hexagonal manganites,” *Nature Materials* **13**, 42–9 (2014).
- ⁹⁶X. Wang, M. Mostovoy, M. G. Han, Y. Horibe, T. Aoki, Y. Zhu, and S.-W. Cheong, “Unfolding of vortices into topological stripes in a multiferroic material,” *Physical Review Letters* **112**, 247601 (2014).
- ⁹⁷H. Tan, C. Xu, M. Li, S. Wang, B.-L. Gu, and W. Duan, “Pressure and strain effects of hexagonal rare-earth manganites: a first-principles study,” *Journal of Physics: Condensed Matter* **28**, 126002 (2016).
- ⁹⁸C. Dubourdieu, G. Huot, I. Gelard, H. Roussel, O. Lebedev, and G. Van Tendeloo, “Thin films and superlattices of multiferroic hexagonal rare earth manganites,” *Philosophical Magazine Letters* **87**, 203–210 (2007).
- ⁹⁹J. Nordlander, M. D. Rossell, M. Campanini, M. Fiebig, and M. Trassin, “Inversion-symmetry engineering in layered oxide thin films,” *Nano Letters* **21**, 2780–2785 (2021).

- ¹⁰⁰J. Nordlander, N. Strkalj, M. Fiebig, and M. Trassin, “Probing ferroic states in oxide thin films using optical second harmonic generation,” *Applied Sciences* **8**, 570 (2018).
- ¹⁰¹M. F. Sarott, E. Gradauskaite, J. Nordlander, N. Strkalj, and M. Trassin, “*In situ* monitoring of epitaxial ferroelectric thin-film growth,” *Journal of Physics: Condensed Matter* **33**, 293001 (2021).
- ¹⁰²N. Kumar, S. Najmaei, Q. Cui, F. Ceballos, P. M. Ajayan, J. Lou, and H. Zhao, “Second harmonic microscopy of monolayer MoS₂,” *Physical Review B* **87**, 161403 (2013).
- ¹⁰³S. Geller, J. B. Jeffries, and P. J. Curlander, “The crystal structure of a new high-temperature modification of YGaO₃,” *Acta Crystallographica Section B Structural Crystallography and Crystal Chemistry* **31**, 2770–2774 (1975).
- ¹⁰⁴C. Pistorius and G. Kruger, “Stability and structure of noncentrosymmetric hexagonal LnInO₃ (Ln = Eu, Gd, Tb, Dy, Ho, Y),” *Journal of Inorganic and Nuclear Chemistry* **38**, 1471–1475 (1976).
- ¹⁰⁵R. Shukla, V. Grover, K. Srinivasu, B. Paul, A. Roy, R. Gupta, and A. K. Tyagi, “Rare earth indates (RE: La–Yb): influence of the synthesis route and heat treatment on the crystal structure,” *Dalton Transactions* **47**, 6787–6799 (2018).
- ¹⁰⁶I. Nodari, A. Alebouyeh, J. Brice, R. Gérardin, and O. Evrard, “Caracterisation de nouveaux ferrites d’indium: In₂Fe₄O₉ et InFeO₃,” *Materials Research Bulletin* **23**, 1039–1044 (1988).
- ¹⁰⁷D. M. Giaquinta, W. M. Davis, and H. C. zur Loye, “Structure of indium iron oxide,” *Acta Crystallographica Section C Crystal Structure Communications* **50**, 5–7 (1994).
- ¹⁰⁸M. Seki, T. Konya, K. Inaba, and H. Tabata, “Epitaxial thin films of InFe₂O₄ and InFeO₃ with two-dimensional triangular lattice structures grown by pulsed laser deposition,” *Applied Physics Express* **3**, 105801 (2010).
- ¹⁰⁹M. E. Holtz, E. S. Padgett, R. Steinhardt, C. M. Brooks, D. Meier, D. G. Schlom, D. A. Muller, and J. A. Mundy, “Dimensionality-induced change in topological order in multiferroic oxide superlattices,” *Physical Review Letters* **126**, 157601 (2021).
- ¹¹⁰P. Vogt and O. Bierwagen, “The competing oxide and sub-oxide formation in metal-oxide molecular beam epitaxy,” *Applied Physics Letters* **106**, 081910 (2015).
- ¹¹¹O. Y. Gorbenko, S. Samoilenkov, I. Graboy, and A. Kaul, “Epitaxial stabilization of oxides in thin films,” *Chemistry of Materials* **14**, 4026–4043 (2002).

- ¹¹²P. Dankov, “Laws of the formation and structure of protective films on metals,” in *Proc.(Doklady) Acad. Sci. USSR*, Vol. 23 (1939) p. 548.
- ¹¹³Y. Hamasaki, T. Shimizu, S. Yasui, T. Taniyama, O. Sakata, and M. Itoh, “Crystal isomers of ScFeO_3 ,” *Crystal Growth & Design* **16**, 5214–5222 (2016).
- ¹¹⁴A. Bosak, A. Kamenev, I. Graboy, S. Antonov, O. Y. Gorbenko, A. Kaul, C. Dubourdieu, J. Senateur, V. Svechnikov, H. Zandbergen, and B. Holländer, “Epitaxial phase stabilisation phenomena in rare earth manganites,” *Thin Solid Films* **400**, 149–153 (2001).
- ¹¹⁵F. Moussa, M. Hennion, J. Rodriguez-Carvajal, H. Moudden, L. Pinsard, and A. Revcolevschi, “Spin waves in the antiferromagnet perovskite LaMnO_3 : A neutron-scattering study,” *Physical Review B* **54**, 15149 (1996).
- ¹¹⁶S. Geller and E. Wood, “Crystallographic studies of perovskite-like compounds. I. Rare earth orthoferrites and YFeO_3 , YCrO_3 , YAlO_3 ,” *Acta Crystallographica* **9**, 563–568 (1956).
- ¹¹⁷O. Madelung, U. Rössler, and M. Schulz, eds., *Ternary Compounds, Organic Semiconductors*, Landolt-Börnstein - Group III Condensed Matter, Vol. 41E (Springer-Verlag, Berlin/Heidelberg, 2000).
- ¹¹⁸M. Robbins, G. Wertheim, A. Menth, and R. Sherwood, “Preparation and properties of polycrystalline cerium orthoferrite (CeFeO_3),” *Journal of Physics and Chemistry of Solids* **30**, 1823–1825 (1969).
- ¹¹⁹B. Dabrowski, S. Kolesnik, A. Baszczuk, O. Chmaissem, T. Maxwell, and J. Mais, “Structural, transport, and magnetic properties of RMnO_3 perovskites ($R = \text{La, Pr, Nd, Sm, }^{153}\text{Eu, Dy}$),” *Journal of Solid State Chemistry* **178**, 629–637 (2005).
- ¹²⁰G. J. McCarthy, P. V. Gallagher, and C. Sipe, “Crystal chemistry of catalyst materials. I. Composition and unit cell parameters of “ REMnO_3 ” phases prepared in air,” *Materials Research Bulletin* **8**, 1277–1284 (1973).
- ¹²¹A. A. Bossak, I. E. Graboy, O. Y. Gorbenko, A. R. Kaul, M. S. Kartavtseva, V. L. Svetchnikov, and H. W. Zandbergen, “XRD and HREM studies of epitaxially stabilized hexagonal orthoferrites RFeO_3 ($R = \text{Eu–Lu}$),” *Chemistry of Materials* **16**, 1751–1755 (2004).
- ¹²²S. Quezel, F. Tcheou, J. Rossat-Mignod, G. Quezel, and E. Roudaut, “Magnetic structure of the perovskite-like compound TbMnO_3 ,” *Physica B+C* **86**, 916–918 (1977).

- ¹²³M. Marezio, J. Remeika, and P. Dernier, “The crystal chemistry of the rare earth orthoferrites,” *Acta Crystallographica Section B: Structural Crystallography and Crystal Chemistry* **26**, 2008–2022 (1970).
- ¹²⁴W. C. Chueh, F. El Gabaly, J. D. Sugar, N. C. Bartelt, A. H. McDaniel, K. R. Fenton, K. R. Zavadil, T. Tyliczszak, W. Lai, and K. F. McCarty, “Intercalation pathway in many-particle LiFePO₄ electrode revealed by nanoscale state-of-charge mapping,” *Nano Letters* **13**, 866–872 (2013).
- ¹²⁵A. Akbashev, V. Roddatis, A. Vasiliev, S. Lopatin, V. Amelichev, and A. Kaul, “Reconstruction of the polar interface between hexagonal LuFeO₃ and intergrown Fe₃O₄ nanolayers,” *Scientific Reports* **2**, 672 (2012).
- ¹²⁶J. Greedan, M. Bieringer, J. Britten, D. Giaquinta, and H.-C. Zur Loye, “Synthesis, crystal structure, and unusual magnetic properties of InMnO₃,” *Journal of Solid State Chemistry* **116**, 118–130 (1995).
- ¹²⁷Y. Bréard, H. Fjellvåg, and B. Hauback, “Investigation of bixbyite type scandium oxides involving a magnetic cation: Sc_{2-x}Fe_xO₃ (0 ≤ x ≤ 1),” *Solid State Communications* **151**, 223–226 (2011).
- ¹²⁸M. F. Bekheet, I. Svoboda, N. Liu, L. Bayarjargal, E. Irran, C. Dietz, R. W. Stark, R. Riedel, and A. Gurlo, “Ferroelectric InMnO₃: Growth of single crystals, structure and high-temperature phase transitions,” *Journal of Solid State Chemistry* **241**, 54–63 (2016).
- ¹²⁹S.-J. Ahn, J.-H. Lee, Y. K. Jeong, E.-H. Na, Y. M. Koo, and H. M. Jang, “Artificially imposed hexagonal ferroelectricity in canted antiferromagnetic YFeO₃ epitaxial thin films,” *Materials Chemistry and Physics* **138**, 929–936 (2013).
- ¹³⁰X. Xu and W. Wang, “Multiferroic hexagonal ferrites (h-RFeO₃, R= Y, Dy-Lu): a brief experimental review,” *Modern Physics Letters B* **28**, 1430008 (2014).
- ¹³¹J. A. Moyer, R. Misra, J. A. Mundy, C. M. Brooks, J. T. Heron, D. A. Muller, D. G. Schlom, and P. Schiffer, “Intrinsic magnetic properties of hexagonal LuFeO₃ and the effects of nonstoichiometry,” *APL Materials* **2**, 012106 (2014).
- ¹³²Y. K. Jeong, J.-H. Lee, S.-J. Ahn, and H. M. Jang, “Epitaxially constrained hexagonal ferroelectricity and canted triangular spin order in LuFeO₃ thin films,” *Chemistry of Materials* **24**, 2426–2428 (2012).
- ¹³³P. Barrozo, D. R. Småbråten, Y. Tang, B. Prasad, S. Saremi, R. Ozgur, V. Thakare, R. A. Steinhardt, M. E. Holtz, V. A. Stoica, L. W. Martin, D. G. Schlom, S. M. Selbach,

- and R. Ramesh, “Defect-Enhanced Polarization Switching in the Improper Ferroelectric LuFeO₃,” *Advanced Materials* **32**, 2000508 (2020).
- ¹³⁴J. Casamento, M. E. Holtz, H. Paik, P. Dang, R. Steinhardt, H. Xing, D. G. Schlom, and D. Jena, “Multiferroic LuFeO₃ on GaN by molecular-beam epitaxy,” *Applied Physics Letters* **116**, 102901 (2020).
- ¹³⁵A. R. Akbashev, V. V. Roddatis, A. L. Vasiliev, S. Lopatin, A. S. Semisalova, N. S. Perov, V. A. Amelichev, and A. R. Kaul, “Reconstructed stacking faults in cobalt-doped hexagonal LuFeO₃ revealed by mapping of cation distribution at the atomic scale,” *CrytEngComm* **14**, 5373–5376 (2012).
- ¹³⁶D. Lee, J.-H. Lee, P. Murugavel, S. Jang, T. Noh, Y. Jo, M.-H. Jung, Y.-D. Ko, and J.-S. Chung, “Epitaxial stabilization of artificial hexagonal GdMnO₃ thin films and their magnetic properties,” *Applied Physics Letters* **90**, 182504 (2007).
- ¹³⁷S. Harikrishnan, S. Rößler, C. N. Kumar, H. Bhat, U. Rößler, S. Wirth, F. Steglich, and S. Elizabeth, “Phase transitions and rare-earth magnetism in hexagonal and orthorhombic DyMnO₃ single crystals,” *Journal of Physics: Condensed Matter* **21**, 096002 (2009).
- ¹³⁸J. Iida, S. Takekawa, and N. Kimizuka, “Single crystal growth of LuFe₂O₄, LuFeCoO₄ and YbFeMgO₄ by the floating zone method,” *Journal of Crystal Growth* **102**, 398–400 (1990).
- ¹³⁹R. A. Steinhardt, C. M. Brooks, G. C. Correa, M. E. Holtz, R. Ramesh, D. A. Muller, J. A. Mundy, and D. G. Schlom, “DyFe₂O₄: A new trigonal rare-earth ferrite grown by molecular-beam epitaxy,” *APL Materials* **9**, 041106 (2021).
- ¹⁴⁰H. Iida, T. Koizumi, Y. Uesu, K. Kohn, N. Ikeda, S. Mori, R. Haumont, P.-E. Janolin, J.-M. Kiat, M. Fukunaga, and Y. Noda, “Ferroelectricity and ferrimagnetism of hexagonal YbFeO₃ thin films,” *Journal of the Physical Society of Japan* **81**, 024719 (2012).
- ¹⁴¹H. Yokota, T. Nozue, S. Nakamura, M. Fukunaga, and A. Fuwa, “Examination of ferroelectric and magnetic properties of hexagonal ErFeO₃ thin films,” *Japanese Journal of Applied Physics* **54**, 10NA10 (2015).
- ¹⁴²Y. Hamasaki, T. Katayama, S. Yasui, T. Shiraishi, A. Akama, T. Kiguchi, T. Taniyama, and M. Itoh, “Switchable third ScFeO₃ polar ferromagnet with YMnO₃-type structure,” *Journal of Materials Chemistry C* **8**, 4447–4452 (2020).
- ¹⁴³J. Li, U. G. Singh, T. D. Schladt, J. K. Stalick, S. L. Scott, and R. Seshadri, “Hexagonal YFe_{1-x}Pd_xO_{3-δ}: Nonperovskite host compounds for Pd²⁺ and their catalytic activity for

CO oxidation,” *Chemistry of Materials* **20**, 6567–6576 (2008).

¹⁴⁴A. A. Belik, S. Kamba, M. Savinov, D. Nuzhnyy, M. Tachibana, E. Takayama-Muromachi, and V. Goian, “Magnetic and dielectric properties of hexagonal InMnO_3 ,” *Physical Review B* **79**, 054411 (2009).

¹⁴⁵B. Paul, S. Chatterjee, S. Gop, A. Roy, V. Grover, R. Shukla, and A. Tyagi, “Evolution of lattice dynamics in ferroelectric hexagonal REInO_3 (RE= Ho, Dy, Tb, Gd, Eu, Sm) perovskites,” *Materials Research Express* **3**, 075703 (2016).

¹⁴⁶U. Adem, A. A. Nugroho, A. Meetsma, and T. Palstra, “Ferroelectric displacements in multiferroic $\text{Y}(\text{Mn,Ga})\text{O}_3$,” *Physical Review B* **75**, 014108 (2007).

VII. A NOTE ON HEXAGONAL GEOMETRY

The effective hexagonal in-plane lattice parameter of a (111)-oriented cubic crystal depends on the type of cubic structure the material forms. The simplest structure is the simple cube. For a crystal with cations on the corners of a cube, the (111) lattice parameter is given by the length of the face diagonal of the cube:

$$a_{hex} = a_{SC}\sqrt{2}$$

Materials that follow this formula include cubic perovskites (e.g. SrTiO_3 , KTaO_3 , and LaAlO_3). Most of the common substrates and bottom electrode materials considered in this review have a face-centered cubic (FCC) structure. For this structure, the hexagonal lattice parameter is given by (1/2) of the face diagonal of the cubic unit cell:

$$a_{hex} = \frac{a_{FCC}\sqrt{2}}{2}$$

Various single elements (e.g. Ir, Pt, Pd, Ag, Si) crystallize in an FCC lattice. Spinel (e.g. MgAl_2O_4) and rock salt-type structures (e.g. MgO) also follow the FCC formula. Other materials with an FCC-type configuration include $\text{SiC}(3C)$, CaF_2 , and Ytria-stabilized Zirconia (YSZ). Some elements crystallize as a body-centered cubic (BCC) lattice (e.g. Cr, Mn, Fe, Mo). The hexagonal lattice parameter for this structure is the length of the face diagonal, just as in the simple cubic case, because the central atom lies slightly out of the (111) plane that includes 3 corner atoms. For the more complicated bixbyite structure, the true (111) lattice parameter follows the simple cubic formula ($a_{hex} = a_{bixbyite}\sqrt{2}$). However,

there are cations in a slightly distorted hexagonal lattice with average spacing $a_{hex}/4$. For this reason, the hexagonal lattice parameter of the bixbyite compound In_2O_3 is reported as 3.58 Å above while the cubic lattice parameter is 10.12 Å, giving 14.31 Å between identical lattice sites in the (111) plane. Other bixbyite materials include $R_2\text{O}_3$, Y_2O_3 , and Mn_2O_3 .

Lattice matching between hexagonal crystals is more complicated than that of cubic or orthorhombic structures. While both structures can accommodate matching between crystals with integer ratios between their parameters (e.g. a and $2a$), hexagonal films can also incorporate scaling factors like $\frac{3}{2}$ or $\frac{4}{3}$ as well as a 30° rotation between the film and substrate. The rotation effectively scales the lattice parameter by $\sqrt{3}$. This possible rotation, along with a scarcity of substrates with proper lattice parameters, complicates studies of strain engineering in hexagonal thin films. As with cubic thin films, the lattice mismatch between substrate and film is quantified as

$$\text{lattice mismatch (\%)} = \frac{a_{sub} - a_{film}}{a_{film}} \times 100$$

For many materials, this simple formula can accurately predict which substrates and films are compatible and how they will align. However, this calculation is imperfect. Especially for large lattice mismatch, the difference in lattice parameters does not tell the whole story. The exact termination of the substrate and structure of the sublattice – the positions and identities of atoms that lie within the cations that define the hexagonal unit cell – can change how the substrate and film will align to reduce energy at the interface. Furthermore the tendency of hexagonal crystals to adopt a 30° rotation or unusual scaling factor between film and substrate complicates the quantification of the lattice mismatch because the alignment can dramatically affect the effective lattice parameter of the substrate.

Below we tabulate the lattice parameters used for substrate and film materials (Table III and Table IV, respectively) shown in Fig. 9.

	Mn			Fe		
	Stable Structure	Epitaxially Stabilized		Stable Structure	Epitaxially Stabilized	
La	$o^{55,115}$	Pbnm		o^{116}	Pbnm	
Ce	o^{117}	Pbnm		o^{118}	Pnma	
Pr	o^{119}	Pbnm		o^{116}	Pbnm	
Nd	$o^{119,120}$	Pbnm		o^{116}	Pbnm	
Sm	$o^{55,120}$	Pnma		o^{116}	Pbnm	
Eu	$o^{119,120}$	Pbnm	h^{66} P6 ₃ cm YSZ(111)	o^{116}	Pbnm	h^{121} P6 ₃ cm YSZ(111)
Gd	o^{120}	Pnma	h^{66} P6 ₃ cm YSZ(111)	o^{116}	Pbnm	
Tb	o^{122}	Pnma		o^{123}	Pbnm	h^{14} P6 ₃ cm YSZ(111)
Dy	$o^{55,119,120}$	Pbnm	h^{66} P6 ₃ cm YSZ(111)	o^{123}	Pbnm	h^{14} P6 ₃ cm YSZ(111)
Ho	$h^{5,120}$	P6 ₃ cm	o^{114} Pnma LAO(001) STO(001)	o^{123}	Pbnm	h^{14} P6 ₃ cm YSZ(111)
Er	$h^{5,55,124}$	P6 ₃ cm		o^{123}	Pbnm	h^{121} P6 ₃ cm YSZ(111)
Tm	$h^{5,120}$	P6 ₃ cm	o^{114} Pnma LAO(001) STO(001)	o^{123}	Pbnm	h^{121} P6 ₃ cm YSZ(111)
Yb	$h^{5,55,120}$	P6 ₃ cm		o^{123}	Pbnm	h^{121} P6 ₃ cm YSZ(111)
Lu	$h^{5,120}$	P6 ₃ cm	o^{114} Pnma LAO(001) STO(001)	o^{123}	Pbnm	$h^{121,125}$ P6 ₃ cm YSZ(111) Al ₂ O ₃ (0001) Fe ₃ O ₄ (111)
Sc	h^{126}	P6 ₃ cm		b^{127}	Ia $\bar{3}$	h^{113} P6 ₃ cm Al ₂ O ₃ (0001)
In	h^{128}	P6 ₃ cm		h^{107}	P6 ₃ / <i>m</i> <i>m</i> <i>c</i>	
Y	$h^{5,55}$	P6 ₃ cm	o Pnma LAO(001) STO(001)	o^{116}	Pbnm	h^{129} P6 ₃ cm Pt(111)

TABLE II. Summary of the $RMnO_3$ and $RFeO_3$ structures where R = rare earth, Sc, In, Y. The bulk stable phase is listed in addition to the structures which can be epitaxially stabilized on the listed substrate or template. o, h, b refer to orthorhombic, hexagonal and bixbyite respectively.

Compound	Orientation	Hexagonal Lattice Constant (\AA)	30° Rotated Lattice Constant (\AA)
$\alpha\text{Al}_2\text{O}_3$	(0001)	4.76	8.24
YSZ	(111)	3.64	6.30
GaN	(0001)	3.19	5.52
SCAM	(0001)	3.25	5.62
4H-SiC	(0001)	3.07	5.32
ZnO	(0001)	3.25	5.63
Graphite	(0001)	2.46	4.26
In_2O_3	(111)	14.31 (3.58)	24.79 (6.20)
CaF_2	(111)	3.86	6.69
KTaO_3	(111)	5.64	9.77
LaAlO_3	(111)	5.37	9.30
MgAl_2O_4	(111)	5.71	9.90
CoFe_2O_4	(111)	3.67	6.36
MgO	(111)	2.98	5.16
3C-SiC	(111)	3.08	5.33
SrTiO_3	(111)	5.52	9.56
Pt	(111)	2.78	4.82
Pd	(111)	2.75	4.76
Ir	(111)	2.72	4.70
Si	(111)	3.84	6.65

TABLE III. Equivalent hexagonal lattice parameters for the substrate materials considered in Fig. 9.

Film	Geometry	Lattice Constant (\AA)	30° Rotated Lattice Constant (\AA)	Reference
YMnO ₃	bulk	6.13		5
GdMnO ₃	thin film	6.30		136
HoMnO ₃	bulk	6.14		5
ErMnO ₃	bulk	6.12		5
TmMnO ₃	bulk	6.06		5
YbMnO ₃	bulk	6.06		5
LuMnO ₃	bulk	6.04		5
TbMnO ₃	thin film	6.27		73
DyMnO ₃	bulk	6.19		137
LuFeO ₃	bulk	5.97		121,125
LuFe ₂ O ₄	bulk	3.43	5.96	138
DyFeO ₃	thin film	6.24		41
DyFe ₂ O ₄	thin film	3.54	6.13	139
YbFeO ₃	thin film	3.46	5.99	140
ErFeO ₃	thin film	6.05-6.09		121,141
ScFeO ₃	thin film	5.72		142
TmFeO ₃	thin film	6.02		121
YFeO ₃	bulk	3.51	6.08	143
InFeO ₃	thin film	3.32	5.75	108
InFe ₂ O ₄	thin film	3.36	5.82	108
InMnO ₃	bulk	5.88		144
YInO ₃	bulk	6.27		145
HoInO ₃	bulk	6.27		145
DyInO ₃	bulk	6.30		145
TbInO ₃	bulk	6.32		145
GdInO ₃	bulk	6.35		145
EuInO ₃	bulk	6.38		145
SmInO ₃	bulk	6.42		145
YGaO ₃	bulk	6.07		146
InGaO ₃	bulk	3.31	5.73	144

TABLE IV. Lattice parameters of known hexagonal ABO_3 compounds.